



Article

Fractal Characteristics of Pore Throat and Throat of Tight Sandstone Sweet Spot: A Case Study in the East China Sea Basin

Wenguang Wang^{1,2,3,*}, Chengyan Lin³ and Xianguo Zhang³¹ Institute of Unconventional Oil & Gas, Northeast Petroleum University, Daqing 163318, China² Key Laboratory of Continental Shale Hydrocarbon Accumulation and Efficient Development, Ministry of Education, Northeast Petroleum University, Daqing 163318, China³ School of Geosciences, China University of Petroleum (East China), Qingdao 266580, China; lincy@upc.edu.cn (C.L.); zhangxianguo@upc.edu.cn (X.Z.)

* Correspondence: wangwenguang.0@163.com or wangwg@nepu.edu.cn

Abstract: The study of the fractal characteristics of the pore throat radius (PTR) and throat radius of sweet spots is crucial for the exploration and development of tight gas sandstone. This study used conventional core analysis, X-ray diffraction analysis, scanning electron microscopy (SEM), and constant-rate mercury injection experiment (CRMI), high-pressure mercury injection experiment (HPMI), and nuclear magnetic resonance (NMR) techniques to investigate the fractal characteristics of the PTR and throat radius of the tight sandstone sweet spots of the Huagang Formation in the central uplift belt of the East China Sea Basin. Based on conventional core analysis and SEM, the main pore types of the tight sandstone samples in the Huagang Formation were determined to be intergranular dissolved pore, intragranular dissolved pore, intergranular pore, and moldic pore. HPMI and NMR techniques were used to evaluate the full-size PTR distribution of type I (TI), type II (TII), and type III (TIII) sweet spots. Based on fractal theory, CRMI was used to calculate the fractal dimension of the PTR and throat radius of three types of sweet spots, and the relationship between the fractal dimensions and pore throat structure parameters and mineral composition were investigated. The results showed that the full-size PTR distribution curve exhibited bimodal or unimodal characteristics. The peak values of the PTR distribution of the TI, TII, and TIII sweet spots were mainly concentrated at 0.002–22.5 μm , 0.001–2.5 μm , and 0.0004–0.9 μm , respectively. The fractal dimensions of the PTR and throat radius were calculated. The average throat radius fractal dimensions of the TI, TIII, and TIII sweet spots were 2.925, 2.875, and 2.786, respectively. The average PTR fractal dimensions of the TI, TII, and TIII sweet spots were 2.677, 2.684, and 2.702, respectively. The throat radius fractal dimension of the TI, TII, and TIII sweet spots was positively correlated with mercury saturation, average throat radius, feldspar content, and clay mineral content and negatively correlated with displacement pressure, quartz content, and carbonate cement content. The PTR fractal dimension of the TI, TII, and TIII sweet spots was positively correlated with displacement pressure, quartz content, and carbonate cement content and negatively correlated with feldspar content. The throat size of the TI sweet spot was large, and the heterogeneity of the throat was strong. The PTR heterogeneity of the TI sweet spot was lower than that of the TII and TIII sweet spots. The findings of this study can provide important guidance for the exploration and development of tight gas sandstone.

Keywords: throat radius; fractal dimension; sweet spot; pore throat radius; tight sandstone

Citation: Wang, W.; Lin, C.; Zhang, X. Fractal Characteristics of Pore Throat and Throat of Tight Sandstone Sweet Spot: A Case Study in the East China Sea Basin. *Fractal Fract.* **2024**, *8*, 684. <https://doi.org/10.3390/fractalfract8120684>

Academic Editor: Alex Elías-Zúñiga

Received: 29 October 2024

Revised: 12 November 2024

Accepted: 19 November 2024

Published: 22 November 2024



Copyright: © 2024 by the authors. Licensee MDPI, Basel, Switzerland. This article is an open access article distributed under the terms and conditions of the Creative Commons Attribution (CC BY) license (<https://creativecommons.org/licenses/by/4.0/>).

1. Introduction

Pore throat structure is a key factor affecting the storage capacity and fluid flow capacity of tight sandstone reservoirs, and it controls the productivity distribution and exploitation efficiency of hydrocarbon reservoirs [1–3]. Tight sandstone reservoirs have poor physical properties, complex pore structures, and strong heterogeneity [4,5]. The main factors determining the reservoir quality are pore throat radius (PTR) and throat radius

distribution, while the flow characteristics of fluids in tight reservoirs largely depend on the difference of microscopic PTR and throat radius. Therefore, a correct understanding of the PTR and throat radius of the tight sandstone sweet spot is of great significance for revealing the storage capacity and seepage capacity of tight gas sandstone reservoirs [2,6–8].

Many techniques and methods have been applied to study the microstructure of tight sandstone, including microscopic observation techniques, fluid injection techniques, and spectroscopic analysis techniques [9–12]. The microscopic observation technique is a qualitative research method for pore throat morphology and size; it can intuitively characterize the geometric characteristics of the pore throat and includes SEM and energy spectrum analysis, secondary electron (SE)/backscattered electron (BSE) imaging, and micro/nano CT scanning [13–15]. Fluid injection techniques, including the constant-rate mercury injection experiment (CRMI), the high-pressure mercury injection experiment (HPMI), nuclear magnetic resonance (NMR), low-temperature nitrogen adsorption, and low-temperature CO₂ adsorption, can quantitatively obtain pore throat size and distribution characteristics [4,16,17]. The spectroscopic analysis techniques mainly include focused ion beam scanning electron microscopy (FIB-SEM), neutron small-angle scattering (SAXS), and X-ray small-angle scattering (SAXS) [11]. However, different experimental techniques differ in the measurement range of the PTR, and these testing techniques all have their advantages and limitations in studying pore throat structures [8,18].

Tight sandstone reservoirs often develop nano-sized and micro-sized pore throats with poor connectivity, and the geometric shapes of pore throats are complex and irregular; so, it is difficult to effectively describe and characterize the microscopic pore throat structure with a single experimental method. Therefore, using various experimental techniques to accurately quantify PTR and throat radius is of great significance for the exploration and development of tight gas sandstone. HPMI can characterize the pore throat structure of a reservoir by testing the relationship between mercury saturation and pressure during the mercury injection process. The T₂ (transverse relaxation time) spectra distribution in low-magnetic-field nuclear magnetic resonance has a direct relationship with the pore structure and can to some extent reflect the full-size PTR distribution of the sample. NMR results are related to the T₂ relaxation time; so, T₂ spectra can only be converted into PTR distribution by combining NMR with other experimental techniques. CRMI can obtain the characteristic parameters of pore throats and throats, which have great advantages in the study of the microscopic pore structure characteristics of tight sandstone. PTR, throat radius, and their fractal characteristics in tight sandstone reservoirs are a naturally complex system. Fractal theory can quantitatively characterize the strong heterogeneity and complexity of pore throat structures in tight sandstone reservoirs [6,19]. Fractal dimension (D) is an important and effective index for elucidating pore structure parameters [10,20]. D can quantify the surface roughness of materials, and the D value of sandstone is usually between 2.0 and 3.0 [21]. The size and structure of the throat affect the microscopic heterogeneity of tight sandstone reservoirs, directly affecting the exploration and development of tight gas sandstone [22].

The tight sandstone reservoir of the Huagang Formation in the East China Sea Basin has undergone complex sedimentary evolution and diagenesis alteration, with a complex pore structure. Wang et al. (2024) used various experimental methods, such as thin sections, SEM, X-ray diffraction analysis, scanning electron microscope mineral quantitative evaluation, and HPMI, and studied the fractal dimension of pore throat structure and the influence of diagenesis on the fractal dimension of the tight sandstone sweet spots of the Huagang Formation in the Jiaying area of the East China Sea Basin [23]. However, the data tested by HPMI show the distribution of pore throat sizes and fail to distinguish between pores and throats. The combination of HPMI and NMR can characterize the full-size PTR distribution of tight sandstone, and CRMI can obtain the PTR and throat radius of tight sandstone. This study is an inheritance and development of previous research and is definitely not a simple repetition. In this study, the full-size PTR distribution of tight sandstone sweet spots is characterized by HPMI and NMR, and the fractal characteristics of

the PTR and throat radius of the tight sandstone sweet spot were investigated by combining fractal theory and the CRMI technique. The main purpose of this study is to: (1) characterize the pore throat morphology and size distribution of tight sandstone sweet spots using SEM, CRMI, HPMI, and NMR; (2) quantitatively evaluate the full-size PTR distribution of the tight sandstone sweet spot by combining HPMI and NMR; (3) calculate the fractal dimension of the PTR and throat radius of the tight sandstone sweet spots using the CRMI results; and (4) investigate the relationship between the fractal characteristics, pore throat structure parameters, and mineral composition. The results of this study can provide valuable guidance for the exploration and development of tight gas sandstone.

2. Samples and Methods

2.1. Geological Background and Samples

The East China Sea Basin is a petroliferous basin located in eastern China (Figure 1a) [24]. The basin is composed of three first-order tectonic units: the eastern depression group, the central uplift group, and the western depression group [25,26]. The Xihu Depression is located in the central part of the eastern depression group of the East China Sea Basin, with an area of approximately 59,000 km². The western side of the Xihu Depression is bounded by the Haijiao uplift and the Yushan uplift; the eastern side is bounded by the Diaoyudao uplift; the northern side is adjacent to the Fujiang Depression; and the southern side is connected to the Diaobei Depression (Figure 1b) [27]. The Xihu Depression is divided from east to west into an eastern fault terrace belt, a central uplift belt, and a western slope belt [28,29]. A gas field is located in the north-central region of the central uplift belt of the Xihu Depression (Figure 1c). The exploration area of A gas field is approximately 229 km², with 4 drilling wells (Figure 1d). The main gas producing layers in the basin are the Huagang Formation and Pinghu Formation. The Huagang Formation can be further divided into 12 subunits from top to bottom, namely the first member—twelfth member (H1–H12). The upper and lower parts of the Huagang Formation are divided into H1–H5 and H6–H12, respectively. According to previous research, the rocks in the upper part of the Huagang Formation belong to braided delta sediments and are the main natural gas reservoirs. The target interval of this study is the tight sandstone of the H4 and H5 members. The burial depth of the tight sandstone of the fourth (H4) and fifth (H5) members in A gas field is approximately 380–4150 m.

The sampling wells were located in A gas field of the East China Sea Basin, and the samples were taken from the tight sandstone reservoirs of the H4 and H5 members of the Huagang Formation. In this study, 1142 conventional core analysis data items and 108 X-ray diffraction analysis data items were collected from the H4 and H5 tight sandstones of the Huagang Formation in the A gas field of the East China Sea Basin. The total length of the core section for the target interval of the four sampling wells was 129.9 m, including 27.1 m for well A1, 48.3 m for well A2, 45.5 m for well A3, and 9.0 m for well A4. The typical sandstone samples of the tight sandstone of the Huagang Formation from wells A1, A2, A3, and A4 in A gas field were selected, and 158 SEM, 6 CRMI, 13 HPMI, and 13 NMR tests were conducted. Six typical cylindrical samples with a diameter of 2.54 cm and a length of 0.5 cm were selected for CRMI. Thirteen typical cylindrical samples with a diameter of 2.54 cm and a length of 2.5 cm were selected for HPMI. The sample information for the 13 HPMI and 13 NMR tests was the same.

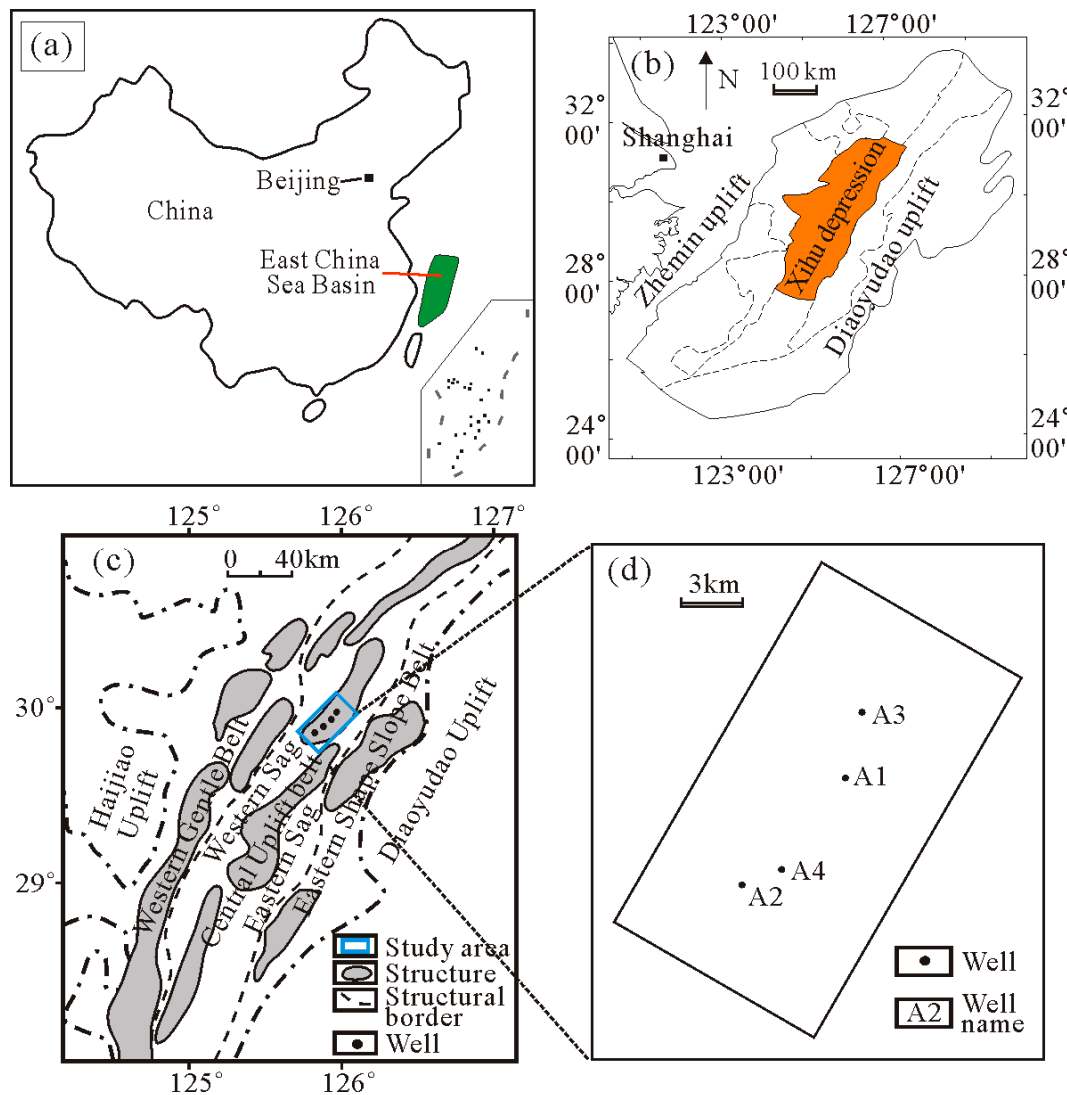


Figure 1. (a) Location of the East China Sea Basin [30]. (b) Location of Xihu Depression. (c) Tectonic unit division of the Xihu Depression and the location of A gas field (modified from [31]). (d) A gas field.

2.2. Experimental Measurements

2.2.1. SEM

A total of 158 gold-plated sandstone bulk samples were selected for SEM analysis. The sandstone sample processing procedure included oil washing, sample selection, piling, drying, dust removal, and gold plating. The manufacturer of Quanta FEG 450 scanning electron microscopy is Financial Executives International company (Hillsborough, OR, USA). The type and morphology of the pore throat and mineral distribution of the tight sandstone were studied using Quanta FEG 450 scanning electron microscopy [32,33].

2.2.2. CRMI

Based on a large number of SEM image observations, a total of six typical tight sandstone sweet spot samples were selected for a constant-rate mercury injection experiment (CRMI). The six samples were composed of three type I (TI) sweet spots, one type II (TII) sweet spot, and two type III (TIII) sweet spots. The manufacturer of the ASPE-730 constant-rate mercury injection instrument is American Core Experimental System Company (Houston, TX, USA). A cylindrical sample with a diameter of 2.54 cm and a length of 0.5 cm was drilled from 6 core samples for CRMI. The experiment was carried out using the ASPE-730 constant-rate mercury injection instrument, which injected mercury into a

core sample at a quasi-static constant rate of 0.0001 mL/min. The temperature was set to 25 °C, the contact angle was 140°, and the interfacial tension was 485 dyn/cm. The maximum mercury injection pressure of the CRMI was 6.201 MPa, and the corresponding throat radius was about 119 nm.

A constant low speed causes the mercury injection process to be approximated as a quasi-static process. Mercury, as a non-wetting phase, is injected into rock pores at an extremely low and constant rate to ensure a constant contact angle and interfacial tension during the experimental process. The capillary resistance reaches the maximum at the minimum radius of the throat. When mercury breaks through the throat and enters the pores, the pressure drops and fills the pores, causing the pressure to rise again. Every change in pore shape experienced by the mercury front leads to a change in the shape of the meniscus, resulting in a change in the capillary pressure of the system. Under the quasi-static mercury injection condition, the microstructure of the pores is determined according to the natural pressure fluctuation of the meniscus at the mercury injection when it passes through different microscopic pore shapes. By using high-precision pressure sensors to record the changes in pressure with the amount of mercury injected, the throat was distinguished from the pores, and the frequency distribution data of the throat radius, PTR, and pore to throat radius ratio were obtained.

2.2.3. HPMI

Based on a large number of SEM image observations, a total of 13 typical tight sandstone sweet spot samples were selected for high-pressure mercury injection experiments (HPMI). The 13 samples were composed of three TI sweet spot, three TII sweet spots, and seven TIII sweet spots. The manufacturer of the AutoPore IV-9520 mercury injection instrument is Micromeritics Instrument Corporation (Norcross, GA, USA). Cylindrical samples with a diameter of approximately 2.54 cm and a length of approximately 4.5 cm were drilled from 13 core samples for HPMI. Before conducting HPMI, oil and gas should be removed from the sample, and the parameters, such as porosity, permeability, and density, should be measured in advance. HPMI was conducted using the AutoPore IV-9520 mercury injection instrument at a temperature of 25 °C and a relative humidity of 35–50%. The sandstone sample underwent oil and gas washing and drying treatment, with a maximum mercury injection pressure of 116.67 MPa and a corresponding PTR of 0.006 μm. During the experiment, the volume accuracy of the mercury entry and exit was greater than 0.1 μL. HPMI can obtain PTR distribution through a capillary pressure curve. The PTR curve (Equation (1)) was obtained by the relationship between capillary pressure and PTR, and the pore structure of the tight sandstone was evaluated.

$$P_c = \frac{2\sigma\cos\theta}{r} \quad (1)$$

where P_c is the capillary pressure, MPa. σ is the surface tension, N/m. In general, $\sigma = 0.48$ N/m. θ is the wetting angle, °. In general, $\theta = 140^\circ$. r is the pore throat radius, μm.

2.2.4. NMR

Based on a large number of SEM image observations, a total of 13 typical tight sandstone sweet spot samples were selected for the NMR experiment. The 13 samples were composed of three TI sweet spots, three TII sweet spots, and seven TIII sweet spots. The manufacturer of the Magnet2000 nuclear magnetic resonance core analyzer is the Institute of Seepage Mechanics, Chinese Academy of Sciences (Beijing, China). Before conducting the NMR experiment, the oil and gas in the sample need to be removed, and porosity and permeability need to be measured in advance. The NMR experiments were carried out on the core samples using the Magnet2000 nuclear magnetic resonance core analyzer. The NMR frequency was 4.99 MHz, the number of echoes was 2048, the waiting time was 4 s, and the echo interval was 0.4 ms. Core samples saturated with water were placed in a low-magnetic-field nuclear magnetic resonance core analyzer for NMR measurement, and

the T_2 relaxation time spectra and T_2 cumulative distribution were calculated by inversion. The core samples after centrifugation (centrifugal force 300 psi = 2.07 MPa) were measured by NMR. The measured parameters were the same as those before centrifugation, and the T_2 relaxation time spectra and T_2 cumulative distribution were calculated by inversion. NMR measurements of the core samples after centrifugation (centrifugal force 300 psi = 2.07 MPa) were performed; the measured parameters were the same as those before centrifugation, and the T_2 relaxation time spectra and T_2 cumulative distribution were calculated by inversion. Then, the $T_{2\text{cut-off}}$ value for each sample was determined. The T_2 spectra of a saturated single-phase fluid can reflect the pore throat structure. Therefore, the T_2 relaxation time can be expressed as Equation (2).

$$\frac{1}{T_2} = \rho_2 \frac{S}{V} \quad (2)$$

where T_2 is the surface relaxation time, ms. ρ_2 is the surface relaxation rate ($\mu\text{ m/ms}$). S/V is the specific surface area, $\mu\text{m}^2/\mu\text{m}^3$.

2.3. Methodology

2.3.1. NMR Movable Fluid Spectrum Conversion

The PTR volume obtained from HPMTI can only characterize a PTR with a large radius. NMR signals can reflect information about the microstructure. In this study, the combination of HPMTI data and NMR data can quantitatively characterize the full-size PTR distribution of tight sandstone. By establishing a mathematical relationship between T_2 relaxation time and throat radius r , the NMR T_2 distribution curve can be converted into a PTR distribution curve [15,34].

For simplified spherical and cylindrical pore structures, the relationship between specific surface area and pore radius can be expressed as follows:

$$\frac{S}{V} = \frac{F_S}{r_c} \quad (3)$$

By combining Equations (2) and (3), Equation (4) is obtained.

$$T_2 = \frac{r_c}{\rho_2 F_S} \quad (4)$$

where F_S is the pore shape factor ($F_S = 3$ for spherical pores and $F_S = 2$ for tubular pores), dimensionless. r_c is the pore radius, μm . Most of the experiment results confirm that T_2 distribution is a power function relationship of the pore radius [35], as shown below.

$$T_2 = \frac{r_c^n}{\rho_2 F_S} \quad (5)$$

where n is a power exponent, dimensionless.

The pore radius r_c is equal to the product of the throat radius and the pore to throat radius ratio, and the relationship between T_2 relaxation time and throat radius can be obtained.

$$T_2 = \frac{(C_1 r_t)^n}{\rho_2 F_S} \quad (6)$$

where C_1 is the average pore to throat radius ratio, dimensionless. r_t is the throat radius, μm .

By defining the following equation:

$$C = \frac{(\rho_2 F_S)^{\frac{1}{n}}}{C_1} \quad (7)$$

we can obtain Equation (8).

$$r_t = CT_2^{\frac{1}{n}} \quad (8)$$

By taking the logarithm on both sides of Equation (8), Equation (9) can be obtained.

$$\ln(r_t) = \ln(C) + \frac{1}{n}\ln(T_2) \quad (9)$$

By fitting the values of C and n , the T_2 spectra of a fully saturated core sample can be converted into a PTR distribution curve.

HPMI was used to convert the NMR T_2 spectra, and the full-size PTR distribution of the tight sandstone was finely characterized. The analytical procedure is as follows. (1) The cumulative amplitude percentage from the large to the small values of the NMR T_2 spectra was calculated. (2) The cumulative mercury saturation percentage of the interpolated HPMI data was calculated from the large to the small PTR. (3) Based on the interpolation relationship between the NMR T_2 spectra data $S(i)$ and HPMI PTR data, the interpolated PTR distribution was obtained (Figure 2a). (4) The left part of black dashed line in Figure 2b was selected as the analysis area. The values of C and n were obtained by fitting the relationship between HPMI interpolated $r(i)$ and NMR $T_2(i)$ in the analysis area by using least square method. The transformation from T_2 relaxation time to PTR can be achieved by substituting C and n into Equation (9).

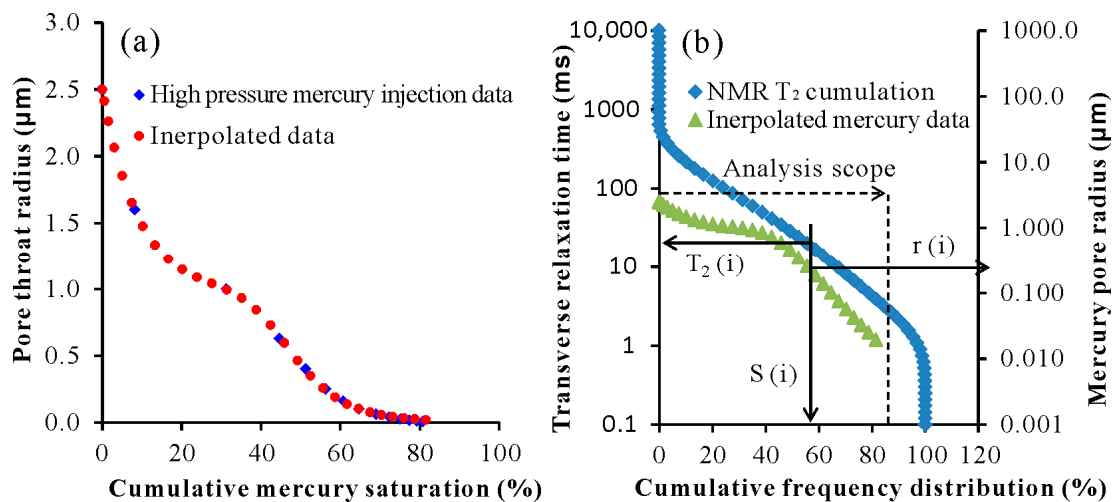


Figure 2. (a) Distribution of PTR and cumulative mercury saturation before and after HPMI interpolation. (b) Conversion from T_2 NMR spectrum distribution curve to PTR distribution curve.

2.3.2. Fractal Method

In a constant-rate mercury injection experiment, capillary pressure can reflect the difficulty of mercury entering the PTR and throat radius. In this study, the fractal dimension of the PTR and throat radius was calculated based on the CRMI data, and the fractal dimension of the PTR and throat radius of tight sandstone were quantitatively characterized. The analytical procedure for calculating the fractal dimension is similar to that reported by [3,23]. The published mercury intrusion capillary pressure model equation can be used to calculate the fractal dimension [3].

$$\lg[1 - S_{Hg}(> r)] = (3 - D)\lg(r) - (3 - D)\lg r_{\max} \quad (10)$$

where D is the “ D ” of MIP. S_{Hg} is mercury saturation, %. r_{\max} is the maximum pore throat radius, measured in μm . r is the pore throat radius, μm .

The fractal dimension D is calculated based on the linear slope λ between $\lg[1 - S_{Hg} (>r)]$ and $\lg(r)$. The fractal dimension can be derived from the slope of a line ($\lambda = 3 - D$), as shown below.

$$D = 3 - \lambda \quad (11)$$

According to fractal theory, pore throat structure fractals can be divided into total fractals and segmented fractals [36]. When the segmented fractal curve of the $\lg(1 - S_{Hg}) - \lg(r)$ curve is not a straight line and has obvious inflection points, the curve can be divided into small and large PTR, and the fractal dimensions of the small and large PTR can be calculated. These two types of pores have obvious inflection points on the $\lg(1 - S_{Hg})$ and $\lg(r)$ curves; then, the fractal dimensions of the small PTR and large PTR are calculated by linear fitting according to the abovementioned fractal dimension calculation procedure. Finally, based on the fractal dimensions and porosity of the small and large PTR, the weighted average method can be used to obtain the fractal dimension (D) of the entire PTR (Equation (12)).

$$D = D_1 \times \frac{\varphi_1}{\varphi_1 + \varphi_2} + D_2 \times \frac{\varphi_2}{\varphi_1 + \varphi_2} \quad (12)$$

where D is the total fractal dimension. D_1 is the fractal dimension of the small pore throat. D_2 is the fractal dimension of the large pore throat. φ_1 is the porosity of the small pore throat, %. φ_2 is the porosity of the large pore throat, %.

Based on the CRMI data, the fractal characteristics of the PTR and throat radius of the sandstone samples were analyzed, and the corresponding fractal dimensions were calculated.

3. Results

3.1. Petrographic Characteristics and Pore Types

The sandstone of the H4 and H5 members in the central uplift belt of the East China Sea Basin is mainly composed of feldspar lithic quartzose, accompanied by a small amount of feldspathic litharenite and litharenite (Figure 3a). The main minerals of these sandstones are quartz, feldspar, and rock fragments, with content ranges of 53.0–75.0%, 8.0–20.0%, and 14.0–37.0%, respectively. The sorting degree of the clastic grains is moderate or good, and the roundness is sub-angular and sub-rounded. Based on bulk rock and clay X-ray diffraction analysis, the content of clay minerals ranges from 2.1% to 35.2%, with an average value of 7.62%. The clay minerals are primarily illite, chlorite, and illite–smectite mixed layers, with a relatively small volume fraction of kaolinite (Figure 3b). Illite has the highest volume fraction, ranging from 0.231% to 15.84%, with an average value of 2.55%. The volume fraction of chlorite is second, ranging from 0.595% to 11.14%, with an average value of 2.44%. The volume fraction of the illite–smectite mixed layer ranges from 0.217% to 15.488%, with an average value of 2.34%. The porosity range of tight sandstone in the H4 and H5 members is 1.2–16.4%, with an average value of 8.27%, and the permeability range is 0.0232–156 mD, with an average value of 1.5 mD.

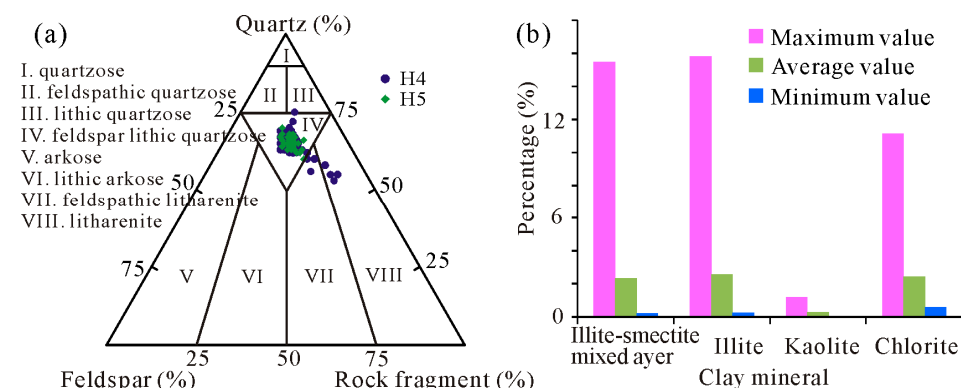


Figure 3. (a) Ternary plot of rock types in the H4 and H5 members of A gas field in East China Sea Basin [37]. (b) Histogram of clay mineral composition.

Under the thin section and SEM, four types of pores were mainly developed in the tight sandstone reservoirs of the H4 and H5 members in the A gas field, including intergranular pores, intergranular dissolved pores, intragranular dissolved pores, and moldic pores (Figure 4). The petrographic data showed that the average percentage contents of the intergranular pores, intergranular dissolved pores, intragranular dissolved pores, and moldic pores were 0.41%, 1.57%, 0.8%, and 0.74%, respectively.

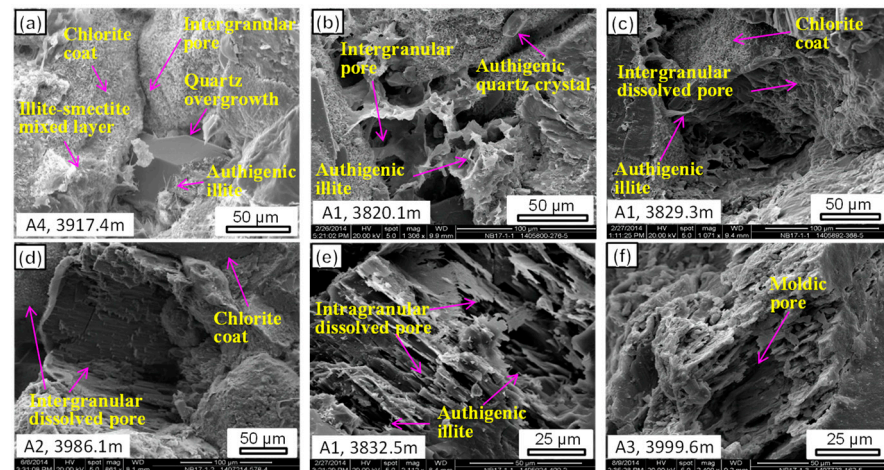


Figure 4. Typical pore types of tight sandstone of the H4 and H5 members in the A gas field. (a) SEM image showing chlorite coat, quartz overgrowth, authigenic illite, and intergranular pores. (b) SEM image showing authigenic illite, authigenic quartz crystals, and intergranular pores. (c) SEM image showing dissolution of debris, intergranular dissolved pores, chlorite coat, and authigenic illite. (d) SEM image showing dissolution of debris, intergranular dissolved pores, chlorite coat, and authigenic illite. (e) SEM image showing dissolution of feldspar, intragranular dissolved pores, and a small amount of authigenic illite. (f) SEM image showing moldic pores and a small amount of authigenic illite.

Intergranular pores are pores between mineral grains after burial diagenesis, typically in the shape of triangles or polygons with smooth straight sides (Figure 4a,b). Most intergranular pores are influenced by diagenesis, such as mechanical compaction and clay mineral cementation filling, forming micro-sized and nano-sized intergranular pores (Figure 4a,b). Intergranular dissolved pores contain some primary intergranular pores, which are the result of further dissolution on the basis of primary intergranular pores (Figure 4c,d). Intergranular dissolved pores are mainly dissolution pores between mineral grains or dissolution pores at mineral edges, accompanied by illite, chlorite, and authigenic quartz. Pores have irregular pore surfaces, ranging in diameter in the order of several hundred micrometers, which provide the main storage space for tight gas sandstones. Intragranular dissolved pores are mainly dissolution pores within the clastic grains, which are further subdivided into feldspar dissolved pores and debris dissolved pores based on the composition of dissolved debris (Figure 4e). A small amount of illite and authigenic quartz is distributed within intragranular dissolved pores, resulting in various types of pores and throats. Moldic pores are dissolution pores where the clastic grains are completely dissolved, leaving only the outer shape (Figure 4f). Illite and authigenic quartz can be seen in the moldic pores.

3.2. Pore Throat Size Distribution Characteristics

3.2.1. Constant-Rate Mercury Injection Experiment Result

CRMI can directly measure the throat radius and the volume distribution controlled by the throat. The pore radius and throat radius distributions were calculated according to the capillary pressure curve of the constant-rate mercury injection experiment (Figure 5 and Table 1). The average pore radius of six typical sandstone samples was mainly distributed

in the range of 124.58–154.63 μm , and the average throat radius was mainly distributed in the range of 0.489–2.669 μm . Figure 5 shows the capillary pressure curves of six typical samples. In the pore area, the trend of the total mercury saturation curve was consistent with the pore mercury saturation curve (Figure 5a). In the pore throat area, mercury saturation was controlled by both the pore and the throat. In the throat area, pore mercury saturation stopped increasing as pressure increased, and the throat contributed to total mercury saturation (Figure 5a).

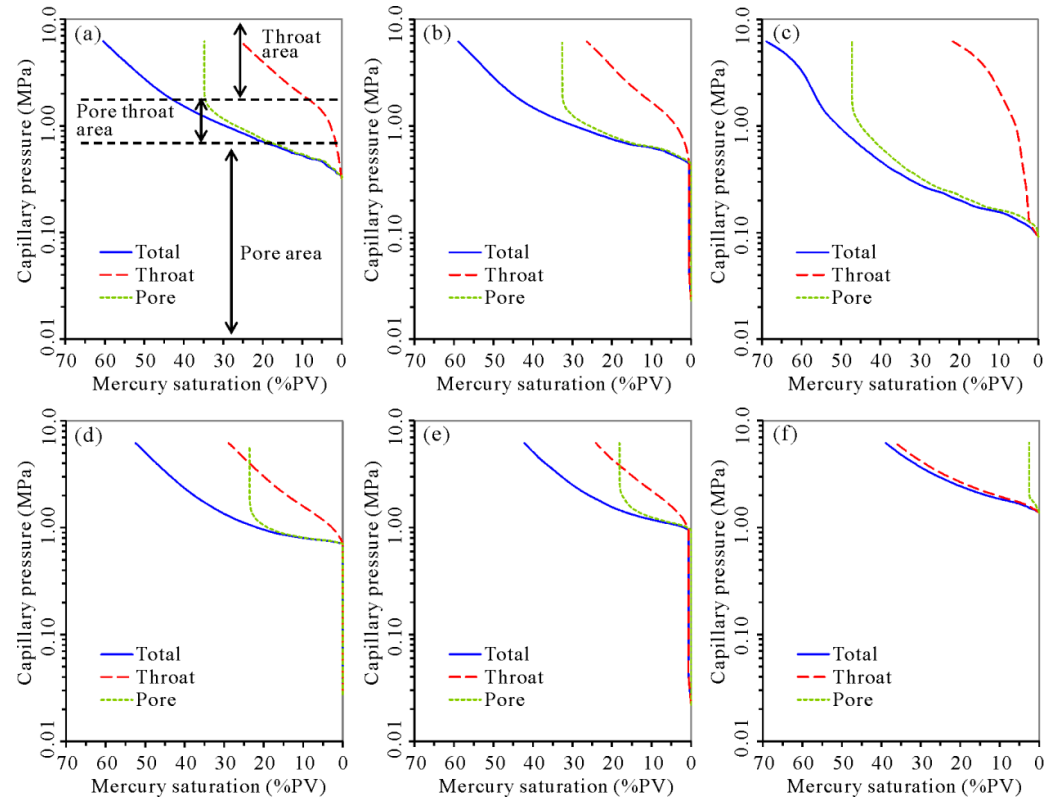


Figure 5. Typical CRMI curve. (a–c) TI sandstone sweet spot samples. (d) TII sandstone sweet spot sample. (e,f) TIII sandstone sweet spot samples.

Table 1. Parameters of constant-rate mercury injection experiment.

Well Name	Depth (m)	Sweet Spot Type	Displacement Pressure (MPa)	Average Throat Radius (μm)	Average Pore Radius (μm)	Average Pore to Throat Radius Ratio	Average Pore Volume (cm^3/g)	Mercury Saturation (%)
A4	3916.5	Type I	0.379	1.007	124.58	155.3	15.82	60.42
A4	3917.9	Type I	0.479	0.937	147.84	190.1	15.82	58.94
A4	3942.5	Type I	0.112	2.669	134.45	99.8	28.82	68.9
A4	3910.4	Type II	0.689	0.855	148.22	195.1	24.79	52.44
A4	3911.7	Type III	1.017	0.611	154.63	294	24.71	42.2
A4	3915.4	Type III	0.689	0.489	129.23	288.3	10.62	38.9

According to the reservoir properties, the classification evaluation criteria of the reservoir “sweet-spot” in the Huangang Formation were established, namely the TI sweet spot ($\Phi > 10\%$, $K > 1$ mD), TII sweet spot ($8\% < \Phi < 10\%$, 0.4 mD $< K < 1$ mD), and TIII sweet spot ($\Phi < 8\%$, $K < 0.4$ mD). Based on the conventional core analysis data and CRMI data, the experimental samples were classified into TI, TII, and TIII (Table 1 and Figure 5). The average displacement pressures of the TI, TII, and TIII sweet spots were 0.323 MPa, 0.689 MPa, and 0.853 MPa, respectively, and the corresponding throat radii were 1.54 μm , 0.855 μm , and 0.55 μm , respectively. The average mercury saturation values of the TI, TII,

and TIII sweet spots were 62.75%, 52.44%, and 40.55%, respectively (Figure 5). Due to the limitation of the experimental principle, the average pore radius calculated from the pore to throat radius ratio was between 100 μm and 300 μm , which is inconsistent with the actual situation.

The throat radius distribution range measured by CRMI was 0.118–6.560 μm (Figure 6a). The average throat radius was positively correlated with permeability (Figure 6b), indicating that the throats affected the permeability of the tight sandstone reservoirs.

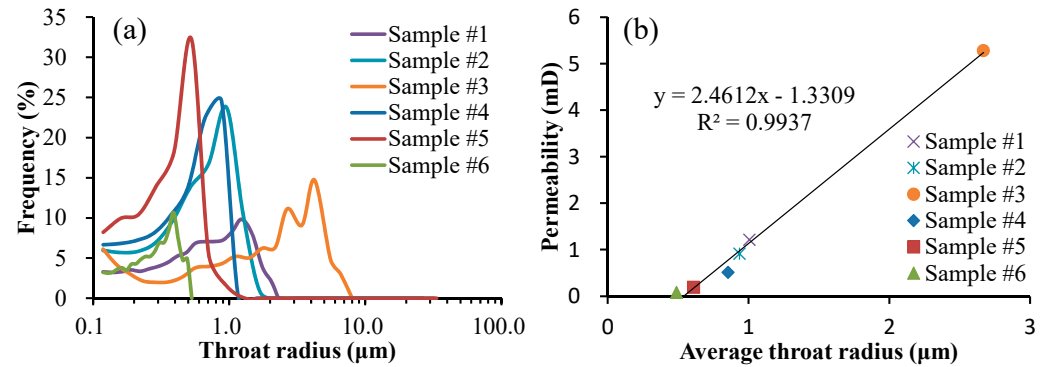


Figure 6. (a) Distribution of throat radius. (b) Relationship between average throat radius and permeability.

3.2.2. High-Pressure Mercury Injection Experiment Result

HPMI can reflect the pore throat structure and pore radius distribution characteristics of tight sandstone. The average displacement pressure and average PTR of the 13 typical sandstone samples were 1.16 MPa and 0.89 μm , respectively (Table 2). The average values of the maximum mercury saturation, relative sorting coefficient, and skewness of the sample were 77.1%, 0.36, and 1.49, respectively (Table 2).

Table 2. Parameters of high-pressure mercury injection experiment.

Well Name	Depth (m)	Porosity (%)	Permeability (mD)	Sweet Spot Type	Maximum Mercury Saturation (%)	Relative Sorting Coefficient	Skewness	Average Pore Throat Radius (μm)	Displacement Pressure (MPa)	Efficiency of Mercury Withdrawal (%)
A2	3971.6	11.3	2.04	Type I	80.66	0.31	2	0.79	0.3	25.98
A4	3915.9	13.1	16	Type I	95.22	0.34	0.96	7.97	0.01	24.21
A4	3918	12.8	2.79	Type I	96.47	0.22	1.09	0.81	0.2	28.46
A2	3976	9.1	0.728	Type II	96.45	0.2	1.53	0.62	0.3	34.72
A2	3983.6	9.2	0.234	Type II	81.61	0.26	1.66	0.17	1.5	38.58
A4	3910.1	9.3	0.441	Type II	81.78	0.28	1.84	0.38	0.3	37.3
A3	3994	5.7	0.134	Type III	69	0.41	1.49	0.14	1.5	44.69
A3	3999.5	7	0.15	Type III	73.67	0.34	1.5	0.13	1.5	42.32
A3	4012.5	5.3	0.108	Type III	69.46	0.4	1.51	0.16	1.5	40.3
A3	4111.2	4.7	0.0598	Type III	57.99	0.57	1.42	0.06	3	45.36
A3	4112.7	4.7	0.076	Type III	62.58	0.5	1.42	0.08	1.5	43.66
A3	4117.2	5.9	0.0804	Type III	70.66	0.38	1.45	0.11	2	43.76
A3	4120.2	6.3	0.146	Type III	66.25	0.45	1.48	0.13	1.5	43.55

The capillary pressure curve can reflect the development and connectivity of connected pore throats and their controlled pore volumes. The mercury injection curve of HPMI was converted into a PTR distribution curve (Figure 7a,b). The PTR and displacement pressure of different types of sweet spots are different to some extent. The average displacement pressures of the TI, TII, and TIII sweet spots were 0.17 MPa, 0.7 MPa, and 1.79 MPa, respectively (Table 2 and Figure 7a). The TI sandstone sweet spot sample had high porosity and permeability, and the capillary curve showed low displacement pressure and a small inclination degree. The TIII sandstone sweet spot samples had low porosity and permeability, and the capillary curves showed high displacement pressure and a large inclination degree (Table 2 and Figure 7a). The PTR ranges of the TI, TII, and TIII sweet spots were

0.0063–63 μm , 0.0063–1.6 μm , and 0.0063–0.4 μm , respectively, with corresponding average values of 3.19 μm , 0.39 μm , and 0.12 μm (Table 2 and Figure 7b).

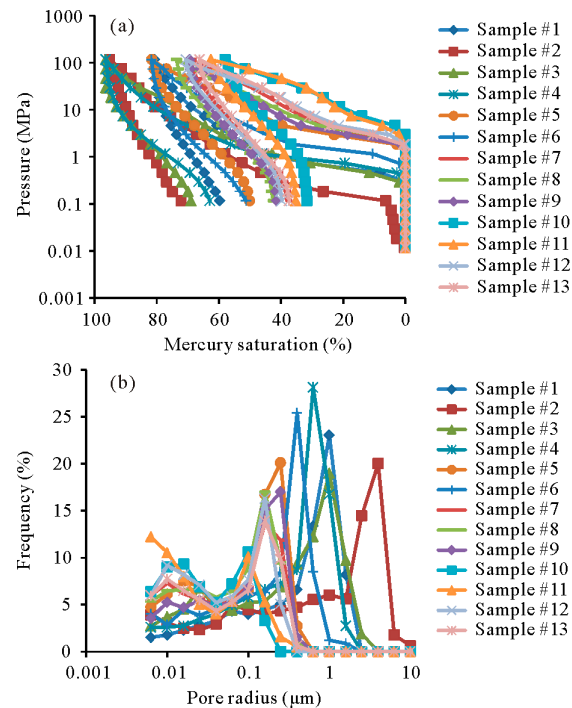


Figure 7. (a) Typical high-pressure mercury injection experiment curves. (b) The characteristics of pore radius of high-pressure mercury injection experiment.

3.2.3. Nuclear Magnetic Resonance Result

The NMR T_2 spectra of fully saturated water samples can reflect the pore throat structure. The T_2 spectra distribution of the 13 samples under fully saturated water conditions revealed bimodal or unimodal characteristics (Figure 8). The T_2 relaxation time was distributed between 0.1 ms and 10,000 ms. Sample # 1, sample # 2, and sample # 3 are sandstone samples of the TI sweet spot. The T_2 spectra distribution of the TI sweet spot showed a bimodal distribution with an obvious right peak, indicating a large pore throat (Figure 8). Sample # 4, sample # 5, and sample # 6 are sandstone samples of the TII sweet spot. The T_2 spectra distribution of the TII sweet spot showed a bimodal distribution with an obvious right peak. However, the right peak amplitude of the TII sweet spot was lower than that of the TI sweet spot (Figure 8). Sample # 7, sample # 8, sample # 9, sample # 10, sample # 11, sample # 12, and sample # 13 are sandstone samples of the TIII sweet spot. The T_2 spectra distribution of the TIII sweet spot showed bimodal characteristics, and the samples with these bimodal characteristics had a wide range of pore throat sizes (Figure 8).

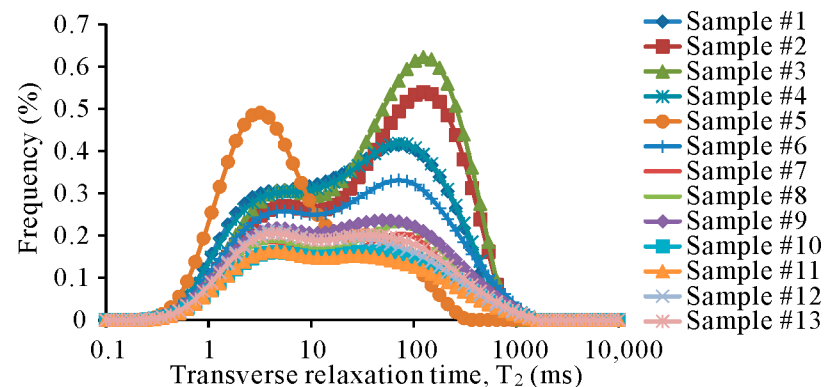


Figure 8. NMR T_2 spectrum of completely saturated water samples.

By placing the porosity cumulative values after centrifugation into the T_2 distribution curve in a fully saturated state, the $T_{2cut-off}$ value was obtained (Figure 9). This cut-off value can be used to separate the movable and irreducible parts of the fluid. In the fully saturated water state, the part of the T_2 distribution curve where T_2 was less than the $T_{2cut-off}$ value can be considered as the irreducible area (indicated by the black diagonal line in Figure 9).

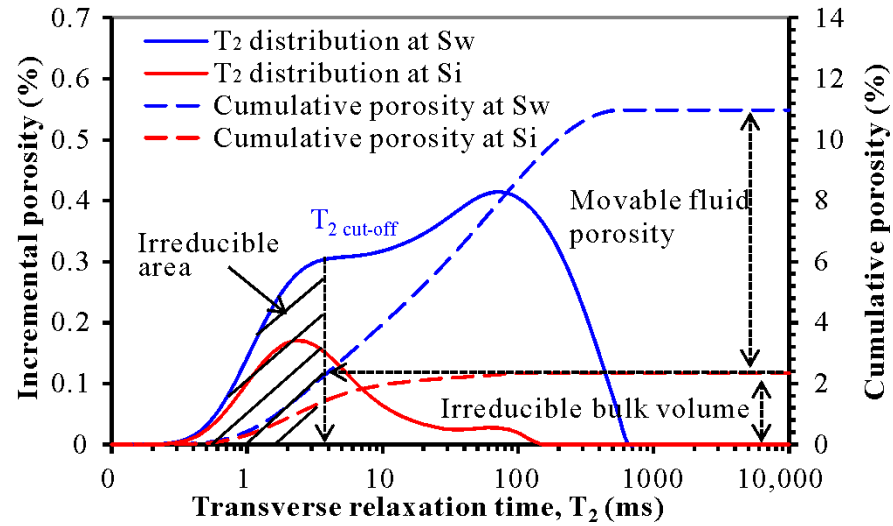


Figure 9. NMR T_2 spectrum of sample # 1 before and after centrifugation.

The $T_{2cut-off}$ values of the 13 samples were distributed between 3.87 ms and 11.57 ms, with an average value of 8.02 ms (Table 3). The average $T_{2cut-off}$ values of the TI, TII, and TIII sweet spots were 7.18 ms, 7.3 ms, and 8.7 ms, respectively (Table 3). The range of the movable fluid saturation of the 13 samples was 42.46–72.06%, with an average value of 57.67%. The average movable fluid saturation values of the TI, TII, and TIII sweet spots were 70.19%, 56.21%, and 52.93%, respectively (Table 3).

Table 3. Parameters of nuclear magnetic resonance experiment.

Sample Number	Well Name	Depth (m)	Sweet Spot Type	$T_{2cut-off}$ (ms)	Movable Fluid Saturation (%)	Movable Fluid Porosity (%)
Sample # 1	A2	3971.6	Type I	3.87	72.06	7.91
Sample # 2	A4	3915.9	Type I	8.03	70.49	8.23
Sample # 3	A4	3918	Type I	9.64	68.02	9.08
Sample # 4	A2	3976	Type II	6.69	67.11	7.43
Sample # 5	A2	3983.6	Type II	5.57	42.46	3.61
Sample # 6	A4	3910.1	Type II	9.64	59.07	5.36
Sample # 7	A3	3994	Type III	6.69	55.85	3.12
Sample # 8	A3	3999.5	Type III	6.69	56.83	3.46
Sample # 9	A3	4012.5	Type III	8.03	57.24	3.98
Sample # 10	A3	4111.2	Type III	11.57	49.24	2.41
Sample # 11	A3	4112.7	Type III	11.57	45.81	2.11
Sample # 12	A3	4117.2	Type III	9.64	49.21	2.9
Sample # 13	A3	4120.2	Type III	6.69	56.34	3.43

3.3. Full-Size Pore Throat Radius Distribution

The full-size PTR distribution was characterized by the combination of HPMI and NMR. In the cross-plot of the T_2 relaxation time and PTR r at the same cumulative distribution frequency, the T_2 and r of the 13 samples showed a distinct two-segment linear relationship and an obvious inflection point (Figure 10a). The least square method was used to fit the C and n values into two segments of the 13 samples, and the results are shown in Table 4. Then, the NMR T_2 spectra could be converted into PTR.

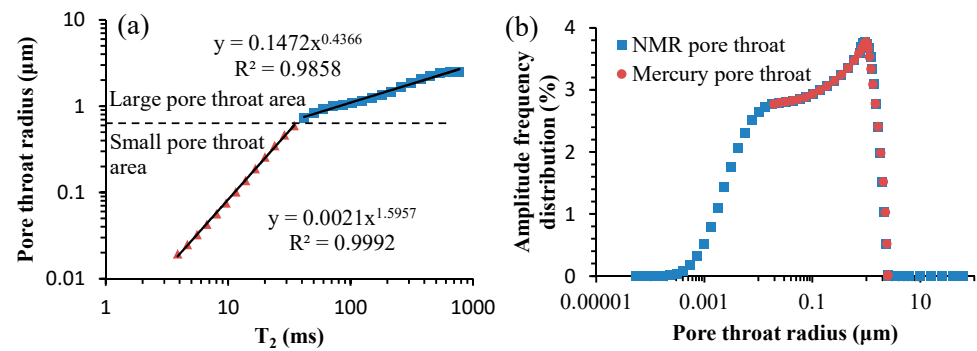


Figure 10. (a) Fitting parameters of NMR T_2 spectrum and PTR for sample # 1 sandstone sample. (b) Comparison between PTR distribution converted from NMR T_2 spectrum of sample # 1 sandstone sample and the HPMI measurement value.

Table 4. Conversion factors between the NMR T_2 spectrum and PTR and the corresponding correlation index.

Sample Number	Well Name	Depth (m)	Sweet Spot Type	Small Pore Throat			Large Pore Throat			Inflection Point (μm)
				C	n	R^2	C	n	R^2	
Sample # 1	A2	3971.6	Type I	0.0021	0.627	0.9992	0.1472	2.29	0.9858	0.65
Sample # 2	A4	3915.9	Type I	0.1795	2.704	0.9803	0.0039	0.726	0.9312	0.87
Sample # 3	A4	3918	Type I	0.0179	1.277	0.9699	0.0046	0.996	0.9091	1.57
Sample # 4	A2	3976	Type II	0.0178	1.024	0.9939	0.1444	2.573	0.9262	0.95
Sample # 5	A2	3983.6	Type II	0.0012	0.43	0.9925	0.0855	3.125	0.8716	0.2
Sample # 6	A4	3910.1	Type II	0.0042	0.971	0.9768	0.0042	1.169	0.9382	0.62
Sample # 7	A3	3994	Type III	0.0009	0.923	0.9976	0.2413	7.764	0.8789	0.49
Sample # 8	A3	3999.5	Type III	0.0013	0.996	0.9979	0.1397	4.983	0.9123	0.42
Sample # 9	A3	4012.5	Type III	0.0012	0.937	0.9994	0.0536	2.723	0.8822	0.27
Sample # 10	A3	4111.2	Type III	0.0004	0.923	0.9996	0.0244	3.238	0.8791	0.1
Sample # 11	A3	4112.7	Type III	0.0003	0.811	0.9993	0.0287	2.866	0.8774	0.13
Sample # 12	A3	4117.2	Type III	0.0011	0.961	0.9995	0.046	3.147	0.8789	0.18
Sample # 13	A3	4120.2	Type III	0.0006	0.86	0.9996	0.0589	3.112	0.8783	0.26

Figure 10b compares the PTR distribution of sample # 1 sandstone sample based on the NMR and HPMI data. The shape and distribution range of the two curves were similar, and the correlation coefficient was very good. The interpolated HPMI data can accurately characterize a part of the PTR distribution, and the PTR distribution characteristics obtained by NMR had a wider distribution range than those obtained by HPMI (Figure 10b). Therefore, by combining NMR and HPMI, the full-size PTR distribution of the entire sample can be effectively characterized.

The full-size PTR distribution of three types of sweet spots was investigated (Figure 11). The distribution range of the PTR was mainly concentrated between 0.0001 μm and 100 μm , and the distribution curve showed bimodal or unimodal characteristics. The PTR distribution curve of the TI sweet spot showed bimodal characteristics, which were mainly distributed in the right peak area, indicating that the PTR was large. The peak value of the PTR distribution of the TI sweet spot was mainly concentrated between 0.002 μm and 22.5 μm (Figure 11). According to the high-pressure mercury injection experiment, the displacement pressures of the sample # 1, sample # 2, and sample # 3 sandstone samples were 0.3 MPa, 0.01 MPa, and 0.2 MPa, respectively, indicating small displacement pressures and large PTR. The permeability of the sample # 1, sample # 2, and sample # 3 sandstone samples was relatively high, which was consistent with the PTR distribution obtained from HPMI and NMR.

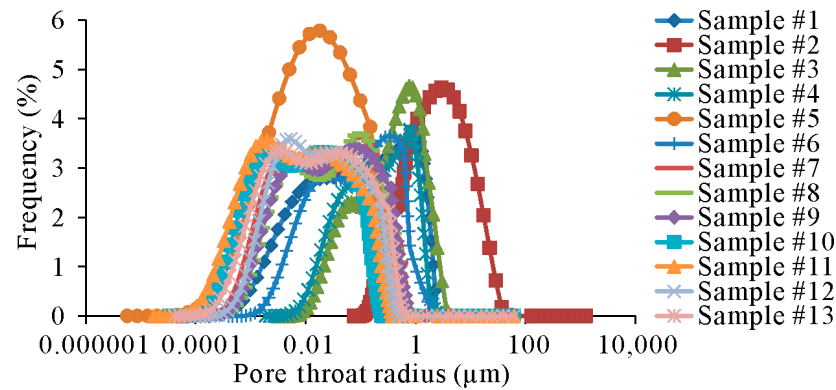


Figure 11. Full-size PTR distribution of tight sandstone in the A gas field of the East China Sea Basin.

Sample # 4, sample # 5, and sample # 6 are sandstone samples of the TII sweet spot. The PTR distribution curves of sample # 4 and sample # 6 had obvious bimodal characteristics, whereas the PTR distribution curve of sample # 5 showed unimodal characteristics. According to the full-size PTR distribution of HPMI and NMR, the peak value of the PTR distribution of the TII sweet spot was mainly concentrated in the range of 0.001–2.5 μm . The PTR distribution curve of the TIII sweet spot showed bimodal characteristics, and the left and right peak areas were similar (Figure 11). According to the full-size PTR distribution of HPMI and NMR, the peak value of the PTR distribution of the TIII sweet spot was primarily concentrated in 0.0004–0.9 μm .

3.4. Fractal Dimension

CRMI data of six sandstone samples were processed; cross-plots of $\lg(1 - S_{Hg}(>r))$ and $\lg(r)$ were constructed, and the slope of the line was fitted. By substituting the slope into Equation (10), the fractal dimensions of the PTR and throat radius of tight sandstone were obtained. The PTR and throat radius of the tight sandstone of the H4 and H5 members in the central uplift belt of the East China Sea Basin are fractal, while the pores of these samples are not fractal (Figure 12). This may be because large pore distribution is not a determinant factor of pore throat structure heterogeneity, and throat distribution is an important factor in pore throat structure heterogeneity.

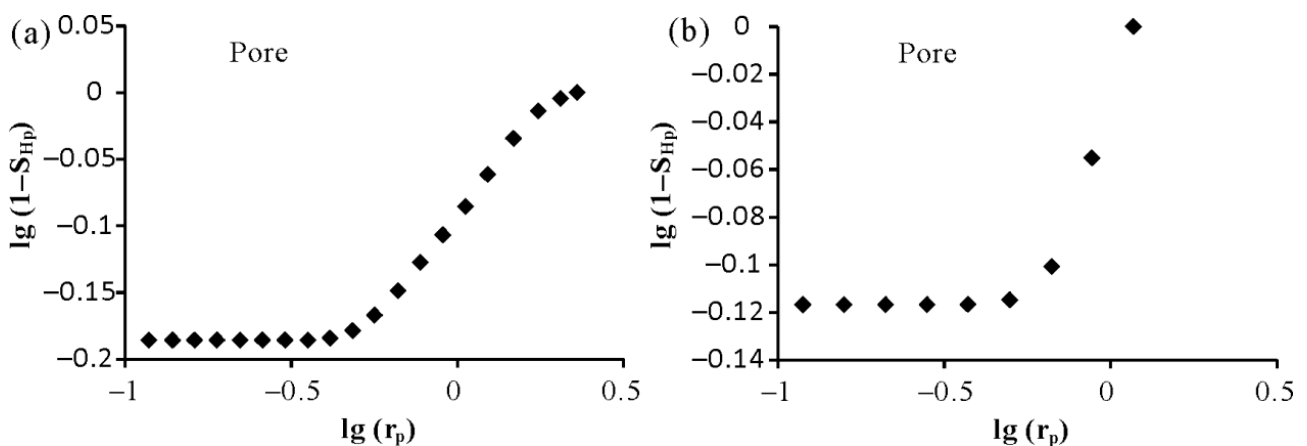


Figure 12. (a) Relationship between $\lg(1 - S_{Hg})$ and $\lg(r)$ of the pores of TI sweet spot. (b) Relationship between $\lg(1 - S_{Hg})$ and $\lg(r)$ of the pores of TII sweet spot.

The fractal characteristics of the PTR and throat radius were investigated (Figure 13). The $\lg(1 - S_{Hg}(>r))$ and $\lg(r)$ curve of the throat radius was clearly divided into two segments at a certain radius, indicating that the tight sandstone sample had a two-segment fractal structure, and the correlation coefficients of the two were greater than 0.9. Figure 13a

shows the fractal curve of the throat radius of the TI sweet spot. The correlation coefficient of the left segment of the curve was 0.9335, corresponding to a small throat. The fractal dimension of the small throat was represented by Dt_1 . The correlation coefficient of the right segment was 0.9998, corresponding to a large throat. The fractal dimension of the large throat was represented by Dt_2 . The $\lg(1 - S_{Hg} (>r))$ and $\lg(r)$ curves of the PTR of the TI sweet spot also showed the fractal characteristics of the two segments (Figure 13b). The correlation coefficient of the left segment of the PTR curve for the TI sweet spot was 0.9871, corresponding to a small pore throat. The fractal dimension of the small pore throat was represented by Dp_1 . The correlation coefficient of the right segment was 0.9994, corresponding to a large pore throat. The fractal dimension of the large pore throat was represented by Dp_2 .

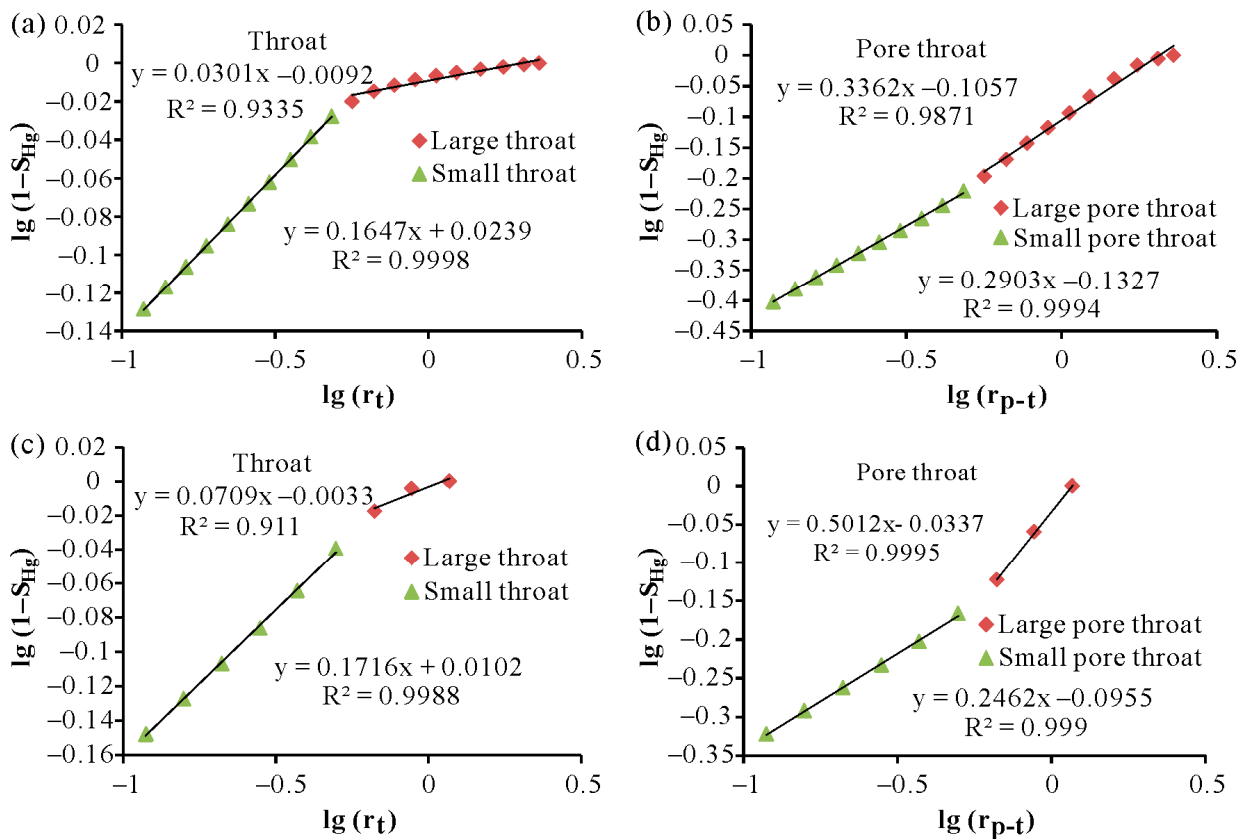


Figure 13. Relationship between $\lg(1 - S_{Hg})$ and $\lg(r)$. (a) TI sweet spot throat radius. (b) TI sweet spot PTR. (c) TII sweet spot throat radius. (d) TII sweet spot PTR.

In most of the samples, the slope of the large throat segment was lower than that of the small throat segment, and the fractal dimension of the large throat segment was larger than that of the small throat segment (Figure 13a,c). The slope of the large pore throat segment was higher than that of the small pore throat segment, and the fractal dimension of the large pore throat segment was smaller than that of the small pore throat segment (Figure 13b,d). This indicated that the heterogeneity of the small throat was lower than that of the large throat, and the heterogeneity of the small pore throat was higher than that of the large pore throat.

The fractal dimensions of the entire PTR and throat radius of six typical sandstone samples were obtained using the weighted average method. The ranges of the fractal dimensions Dt and Dp of the throat radius and PTR were 2.691–2.954 and 2.648–2.749, respectively, and the corresponding average values were 2.87 and 2.69, respectively. The average fractal dimensions of the throat radius of the TI, TII, and TIII sweet spots were 2.925, 2.875, and 2.786, respectively (Table 5), indicating that the throat structure complexity

of the TI sweet spot was higher than that of the TII and TIII sweet spots. The average fractal dimensions of the PTR of the TI, TII, and TIII sweet spots were 2.677, 2.684, and 2.702, respectively (Table 5), and the pore throat structure complexity of the TI sweet spot was lower than that of the TII and TIII sweet spots. The fractal dimension can quantitatively reflect the complexity and heterogeneity of pore throat structure.

Table 5. Fractal dimension calculation of PTR and throat radius.

Well Name	Depth (m)	Sweet Spot Type	Dt_1	R^2	Dt_2	R^2	Dt	Dp_1	R^2	Dp_2	R^2	Dp
A4	3916.5	Type I	2.835	0.9998	2.97	0.9335	2.916	2.71	0.9994	2.664	0.9871	2.682
A4	3917.9	Type I	2.848	0.9994	2.958	0.927	2.905	2.738	0.9982	2.566	0.9754	2.648
A4	3942.5	Type I	2.904	0.9344	2.98	0.9094	2.954	2.762	0.9566	2.671	0.992	2.702
A4	3910.4	Type II	2.828	0.9988	2.929	0.911	2.875	2.754	0.999	2.499	0.9995	2.684
A4	3911.7	Type III	2.833	0.999	2.953	0.8459	2.88	2.777	0.9972	2.706	0.8423	2.749
A4	3915.4	Type III	2.732	0.9969	2.649	0.9828	2.691	2.722	0.997	2.587	0.9885	2.655

4. Discussion

4.1. Full-Size Pore Throat Radius Distribution Characteristics

There are various methods for characterizing pore throat structure, including field emission scanning electron microscopy [38], the gas adsorption method [39], the mercury injection method [40], and nuclear magnetic resonance [34]. Each method has its unique advantages and disadvantages, and it is necessary to combine multiple methods to reveal the full-size pore size distribution of tight reservoirs [41,42]. Previous scholars carried out a large number of studies on full-size pore size characterization, including (1) splicing the pore radius or PTR distributions obtained by low-temperature CO₂ adsorption, low-temperature nitrogen adsorption, and HPMI [39,41]; (2) the characterization of full-size pore size distribution by combining low-temperature nitrogen adsorption and NMR results [43,44]; (3) the study of full-size PTR distribution by combining HPMI and NMR [3]; and (4) quantitatively revealing pore size distribution based on large-field scanning electron microscopy and image recognition techniques [38].

The PTR distribution range of the H4 and H5 tight sandstone in the central uplift belt of the East China Sea Basin is 0.0001–100 μm, and the pore throat structure is complex, which makes it difficult to completely characterize the large-scale PTR distribution in any single experiment. Therefore, combining the results of NMR, low-temperature nitrogen adsorption, HPMI, and CRMI is an effective method for characterizing the full-size PTR distribution of tight sandstone. This study comprehensively applied SEM, HPMI, and NMR techniques, and established a characterization method for the full-size PTR distribution of sweet spots in tight sandstone. By comparing the PTR distribution obtained from HPMI with the cumulative distribution curve of NMR T₂ spectra, HPMI can only characterize large pore throats, and it was difficult for it to reveal many small pore throats. The main peak of the HPMI PTR distribution corresponded to the right peak of the NMR T₂ spectra, and the T₂ spectra were converted into the full-size PTR distribution. The basis for determining the full-size PTR distribution of tight sandstone is as follows. The splicing point between HPMI and NMR was selected at a PTR of 0.1–1.57 μm (Table 4). The distribution of PTR larger than the splicing point was obtained by HPMI. Based on the PTR distribution obtained by NMR and the PTR distribution obtained by HPMI, the distribution of PTR smaller than the splicing point was obtained.

This study combined the results of HPMI and NMR, and quantitatively characterized the full-size PTR distribution of tight sandstone sweet spots. The full-size PTR distribution results of the 13 typical sandstone samples showed that the full-size PTR distribution ranges of the TI, TII, and TIII sweet spots were 0.0004–1265.5 μm, 0.000006–63 μm, and 0.000015–63 μm, respectively (Figure 11), with corresponding the PTR distribution peaks mainly concentrated in 0.002–22.5 μm, 0.001–2.5 μm, and 0.0004–0.9 μm.

4.2. Relationship Between Fractal Dimension and Pore Throat Structure Parameters

Fractal theory is an effective tool to quantitatively characterize the strong heterogeneity and complexity of pore throat structures in tight sandstone reservoirs [19]. All the methods for characterizing the pore throat structure of tight sandstone reservoirs can be used to obtain the fractal dimension of porous rock by establishing fractal models [45]. Previous scholars have carried out a large number of studies on the pore throat structure of tight sandstone, including (1) the fractal dimension derived from complex pore networks obtained from two-dimensional scaled thin sections, SEM, and three-dimensional scaled micro- and nano-CT images [46]; (2) the fractal dimension obtained based on the gas adsorption method [47,48]; (3) the fractal dimension derived from mercury injection capillary pressure data [3,6,15,49]; and (4) the fractal dimension obtained based on nuclear magnetic resonance [9,15]. Wu et al. (2022) studied the pore throat structure and fractal characteristics of Permian Shihezi tight sandstone in Sulige Area, Ordos Basin, by using various experiments involving thin section, SEM, a mercury injection porosimeter, and nuclear magnetic resonance [15]. Based on fractal theory, the fractal dimension of sandstone pore throats was evaluated using HPMI, CRMI, and NMR. Qu et al. (2020) used CRMI results to study the fractal characteristics of pore throats and throats and the relationship between the fractal characteristics and pore throat structure parameters, fluid permeability characteristics, and mineral composition [3]. However, the fractal characteristics of PTR and throat radius in tight sandstone deserts are rarely reported in current studies. Based on the fractal theory, this study used the CRMI results to study the fractal characteristics of the PTR and throat radius of three types of sweet spots in tight sandstone.

With the increase in fractal dimension, the heterogeneity of tight sandstone increases, and the pore throat structure becomes more complex. In order to investigate the relationship between the fractal dimension and pore throat structure parameters of tight sandstone, the intersection analysis of the fractal dimensions D_t and D_p were carried out with mercury saturation, displacement pressure, and average throat radius as parameters (Figure 14). The fractal dimension D_t of the TI, TII, and TIII sweet spots was positively correlated with the mercury saturation (Figure 14a). The fractal dimension D_t and mercury saturation of the TI sweet spot were larger than that of the TII and TIII sweet spots, indicating that the mercury saturation gradually decreased from the TI to the TIII sweet spots (Figure 14a). The fractal dimension D_p of the TI, TII, and TIII sweet spots showed a weak negative correlation with the mercury saturation (Figure 14b).

The fractal dimension D_t of the TI, TII, and TIII sweet spots showed a weak negative correlation with the displacement pressure, whereas the fractal dimension D_p showed a weak positive correlation with the displacement pressure (Figure 14c,d). The displacement pressure of the TI sweet spot was lower than that of the TII and TIII sweet spots. The fractal dimension D_t of the TI, TII, and TIII sweet spots was positively correlated with the average throat radius, whereas the fractal dimension D_p was negatively correlated with the average throat radius (Figure 14e,f). The correlation between the fractal dimension of the throat radius and the average throat radius was higher than that between the fractal dimension of the PTR and the average throat radius. The average throat radius and fractal dimension D_t of the TI sweet spot were high, and the average throat radius and fractal dimension D_t of the TIII sweet spot were low, which indicated that the throat size of the TI sweet spot was large and the heterogeneity of the throat was strong and that there are multiple pore throat shapes.

The fractal dimension D_t of the throat gradually decreased from the TI and TII sweet spots to the TIII sweet spot, indicating that the throat heterogeneity of the TI sweet spot was larger than that of the TII and TIII sweet spots. In contrast, the fractal dimension D_p of the PTR gradually increased or was not significant from the TI and TII sweet spots to the TIII sweet spot, indicating that the heterogeneity of PTR increased or was not significant from the TI and TII sweet spots to the TIII sweet spot.

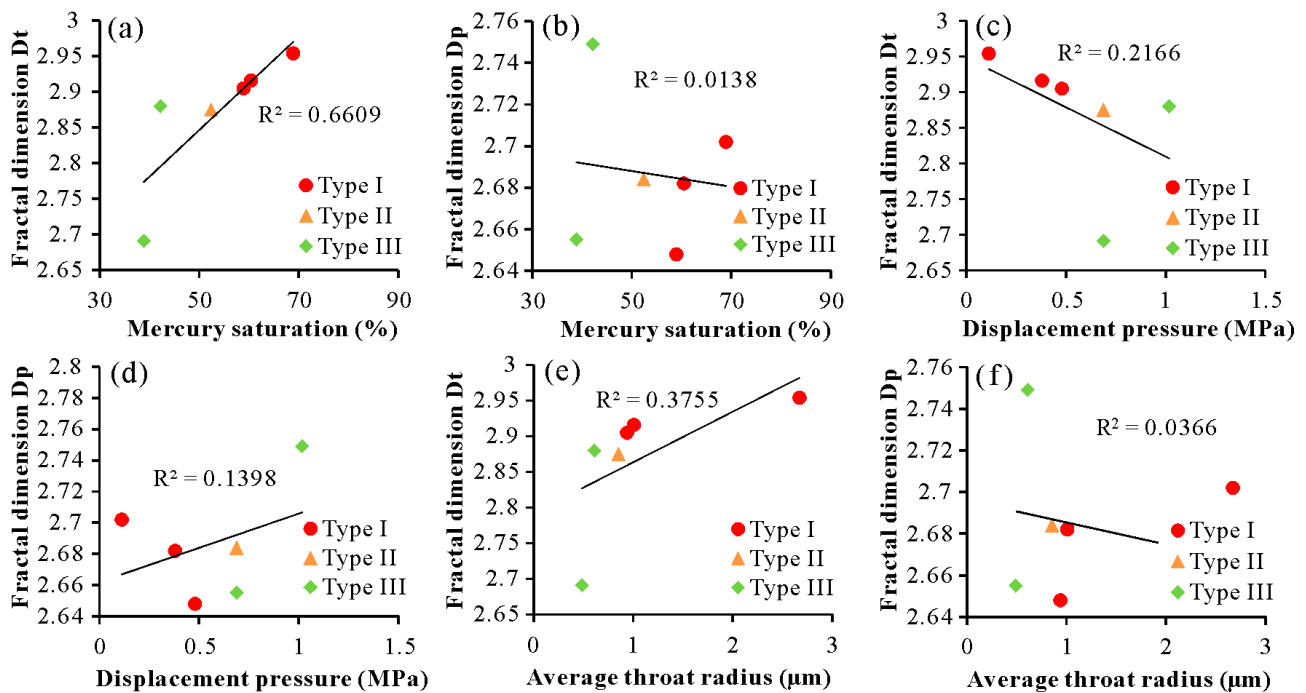


Figure 14. Relationship between throat radius fractal dimension (Dt), PTR fractal dimension (Dp), and pore throat structure parameters. (a) Relationship between fractal dimension Dt and mercury saturation. (b) Relationship between fractal dimension Dp and mercury saturation. (c) Relationship between fractal dimension Dt and displacement pressure. (d) Relationship between fractal dimension Dp and displacement pressure. (e) Relationship between fractal dimension Dt and average throat radius. (f) Relationship between fractal dimension Dp and average throat radius.

4.3. Effect of Mineral Composition on Fractal Dimension

Correlation analysis of mineral composition and fractal dimension was performed (Figures 15 and 16), and the influence of mineral composition and content on the fractal dimension of pore throat structure was investigated. The fractal dimension Dt of the TI, TII, and TIII sweet spots was negatively correlated with quartz content (Figure 15a), whereas the fractal dimension Dp was weakly positively correlated with quartz content (Figure 15b). The negative correlation between the fractal dimension Dt of the throat and the quartz content indicated that the quartz mineral content can improve the throat heterogeneity of tight sandstone to some extent. Quartz minerals had strong anti-compaction and anti-dissolution properties, making the pore throat surface smooth. With the increase in quartz content, the throat heterogeneity of the TI sweet spot was larger than that of the TII and TIII sweet spots. The weak positive correlation between fractal dimension Dp and quartz content can be attributed to the fact that the fractal dimension increased with the increase in quartz content.

The fractal dimension Dt of the TI, TII, and TIII sweet spots was positively correlated with the feldspar content (Figure 15c), whereas the fractal dimension Dp was weakly negatively correlated with the feldspar content (Figure 15d). The positive correlation between fractal dimension Dt and the feldspar content can be attributed to the dissolution of the feldspar, which produced many pores and throats, increasing the throat heterogeneity. If dissolution occurred in the cleavage direction of the feldspar minerals, this created a series of pore throats and increased the heterogeneity of the pore throats. The weak negative correlation between fractal dimension Dp and the feldspar content indicated that the PTR heterogeneity of the TI sweet spots was lower than that of the TII and TIII sweet spots with the increase in feldspar content.

The fractal dimension Dt was negatively correlated with the content of carbonate cement, whereas the fractal dimension Dp was weakly positively correlated with the

content of carbonate cement (Figure 15e,f). The carbonate cement mainly occupied pore space rather than throats, and the carbonate cement increased the heterogeneity of the pore throat structure. The fractal dimension D_t was positively correlated with clay mineral content (Figure 16a), whereas the fractal dimension D_p was negatively correlated with clay mineral content (Figure 16b). The increase in clay mineral content reduced intergranular pores, increased throat radius heterogeneity, and reduced PTR heterogeneity.

In summary, from the TI and TII sweet spots to the TIII sweet spot, the throat radius fractal dimension decreased with increasing quartz content, whereas the PTR fractal dimension increased with increasing quartz content. Due to the dissolution of feldspar, the increase in throat radius heterogeneity, and the decrease in PTR heterogeneity, the fractal dimension of the throat radius increased with the increase in feldspar content, whereas the fractal dimension of the PTR decreased with the increase in feldspar content. Considering that carbonate cement occupied pore space, the fractal dimension of the PTR increased with the increase in carbonate cement content. The weak positive correlation between throat fractal dimension D_t and clay mineral content can be attributed to the complex contact between grains and fillings.

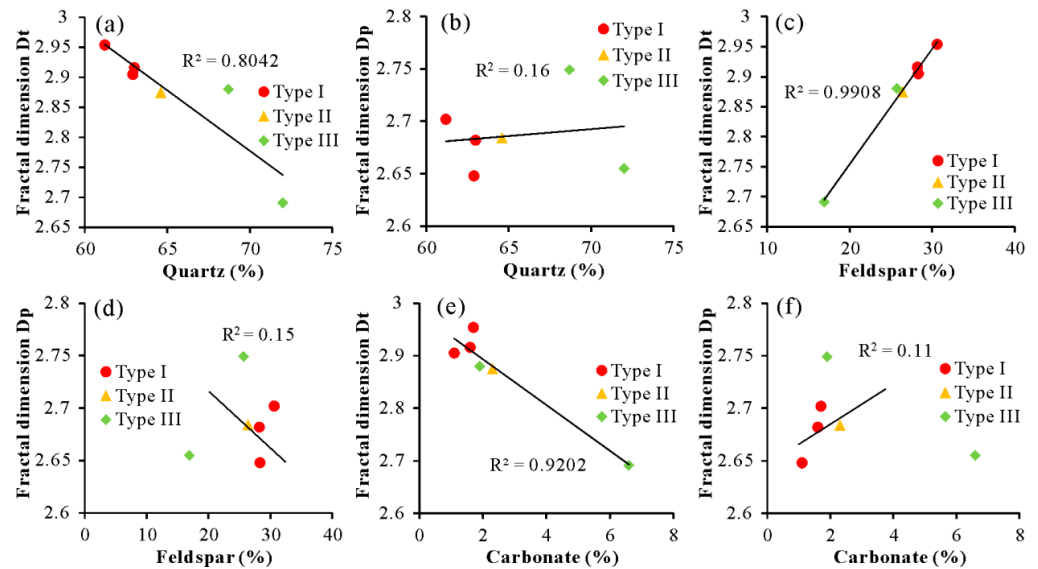


Figure 15. (a) Relationship between throat radius fractal dimensions (D_t) and quartz. (b) Relationship between PTR fractal dimensions (D_p) and quartz. (c) Relationship between fractal dimensions D_t and feldspar. (d) Relationship between fractal dimensions D_p and feldspar. (e) Relationship between fractal dimensions D_t and carbonate cement. (f) Relationship between fractal dimensions D_p and carbonate cement.

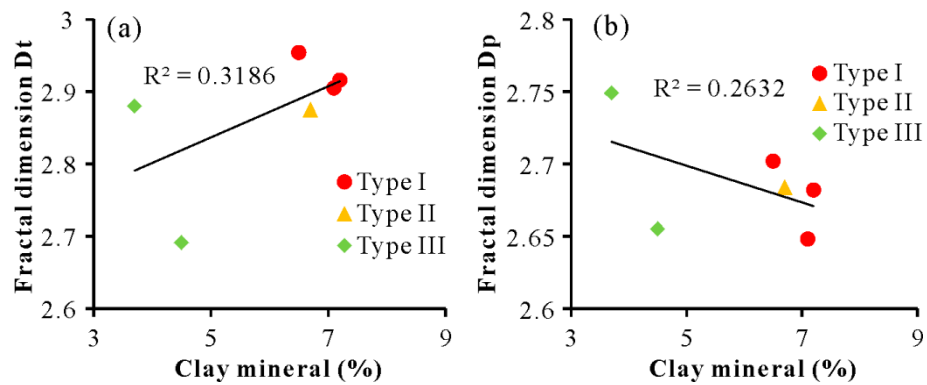


Figure 16. (a) Relationship between fractal dimension D_t and clay minerals. (b) Relationship between fractal dimension D_p and clay minerals.

5. Conclusions

This study used HPMI to convert NMR T_2 spectra and accurately characterized the full-size PTR distribution of tight sandstone sweet spots. In addition, combined with fractal theory, the fractal characteristics of the PTR and throat radius of tight sandstone sweet spots were quantitatively characterized. The conclusions are summarized as follows.

- (1) The tight sandstones of the H4 and H5 members were mainly composed of feldspathic quartzose and a small amount of feldspathic litharenite and litharenite. The porosity range of these tight sandstones was 1.2–16.4%, with an average value of 8.27%. The permeability range was 0.0232–156 mD, and the average value was 1.5 mD. The most common pore types in the research area were feldspar dissolved pores and debris dissolved pores, followed by intragranular dissolved pores, intergranular pores, and moldic pores.
- (2) The average throat radius of the CRMI was mainly distributed between 0.489 μm and 2.669 μm , and the average throat radii of the type I (TI), type II (TII), and type III (TIII) sweet spots were 1.54 μm , 0.855 μm , and 0.55 μm , respectively. The average PTR of the HPMI was mainly distributed between 0.06 μm and 7.97 μm , and the average PTRs of the TI, TII, and TIII sweet spots were 3.19 μm , 0.39 μm , and 0.12 μm , respectively. The average $T_{2\text{cut-off}}$ values of the TI, TII, and TIII sweet spots were 7.18 ms, 7.3 ms, and 8.7 ms, respectively. A characterization method for the full-size PTR distribution of the tight sandstone sweet spots was established by integrating HPMI and NMR techniques, and the full-size PTR distribution of the three types of sweet spots was determined. The full-size PTR distribution curve exhibited bimodal or unimodal characteristics, and the peak values of the PTR distribution of the TI, TII, and TIII sweet spots were mainly concentrated in 0.002–22.5 μm , 0.001–2.5 μm , and 0.0004–0.9 μm .
- (3) Based on fractal theory, the fractal dimensions of the entire PTR and throat radius were calculated. The throat can be divided into two segments, and the average fractal dimensions Dt_1 and Dt_2 of the small throat and large throat were 2.83 and 2.907, respectively. Similarly, the pore throats can be divided into two segments, and the average fractal dimensions Dp_1 and Dp_2 of the small and large pore throats were 2.74 and 2.65, respectively. The ranges of the fractal dimensions Dt and Dp of the throat radius and PTR were 2.691–2.954 and 2.648–2.749, respectively. The average throat radius fractal dimensions of the TI, TII, and TIII sweet spots were 2.925, 2.875, and 2.786, respectively. The average PTR fractal dimensions of the TI, TII, and TIII sweet spots were 2.677, 2.684, and 2.702, respectively.
- (4) The throat radius fractal dimension of the TI, TII, and TIII sweet spots was positively correlated with mercury saturation and average throat radius, and negatively correlated with displacement pressure. The PTR fractal dimension of the TI, TII, and TIII sweet spots was positively correlated with displacement pressure. The throat radius fractal dimension, mercury saturation, and average throat radius of the TI sweet spot were larger than that of the TII and TIII sweet spots, indicating that the throat radius heterogeneity of the TI sweet spot was greater than that of the TII and TIII sweet spots. The PTR fractal dimension of the TI sweet spot was smaller than that of the TII and TIII sweet spots, and the heterogeneity of the PTR increased or was not significant from the TI and TII sweet spots to the TIII sweet spot.
- (5) The effect of mineral composition on the fractal dimension was elaborated. The throat radius fractal dimension of the TI, TII, and TIII sweet spots was negatively correlated with quartz content and carbonate cement content, and positively correlated with feldspar content and clay mineral content. The PTR fractal dimension of the TI, TII, and TIII sweet spots was positively correlated with quartz content and carbonate cement content, and negatively correlated with feldspar content and clay mineral content. With the increase in quartz content, the throat radius heterogeneity of the TI sweet spot was greater than that of the TII and TIII sweet spots. The PTR fractal dimension increased with the increase in quartz content. The dissolution of feldspar

produced many pores and throats, which increased the throat radius heterogeneity. With the increase in feldspar content, the PTR heterogeneity from the TIII and TII sweet spots to the TI sweet spot gradually decreased. The carbonate cement mainly occupied the pore space, and the heterogeneity of the PTR increased with the increase in carbonate cement content. The increase in clay minerals complicated the throat radius heterogeneity.

Author Contributions: Conceptualization, W.W.; Methodology, W.W.; Software, W.W.; Validation, W.W.; Formal analysis, W.W.; Investigation, W.W., C.L. and X.Z.; Resources, W.W., C.L. and X.Z.; Data curation, W.W.; Writing—original draft, W.W., C.L. and X.Z.; Writing—review & editing, W.W., C.L. and X.Z.; Visualization, W.W.; Supervision, W.W.; Project administration, W.W., C.L. and X.Z.; Funding acquisition, W.W. All authors have read and agreed to the published version of the manuscript.

Funding: This research was co-funded by the National Natural Science Foundation of China (grant number: 42202144), the Innovative Research Groups of the National Natural Science Foundation of China (grant number: U19B2006), and the Natural Science Foundation of Shandong Province (grant number: ZR2022QD048).

Data Availability Statement: Data is contained within the article.

Conflicts of Interest: The authors declare no conflict of interest.

References

1. Golab, A.N.; Knackstedt, M.A.; Averdunk, H.; Senden, T.; Butcher, A.R.; Jaime, P. 3D porosity and mineralogy characterization in tight gas sandstones. *Lead Edge* **2010**, *29*, 1476–1483. [[CrossRef](#)]
2. Yao, Y.B.; Liu, D.M. Comparison of low-field NMR and mercury intrusion porosimetry in characterizing pore size distributions of coals. *Fuel* **2012**, *95*, 152–158. [[CrossRef](#)]
3. Qu, Y.Q.; Sun, W.; Tao, R.D.; Luo, B.; Chen, L.; Ren, D.Z. Pore-throat structure and fractal characteristics of tight sandstones in Yanchang Formation, Ordos Basin. *Mar. Pet. Geol.* **2020**, *120*, 104573. [[CrossRef](#)]
4. Clarkson, C.R.; Freeman, M.; He, L.; Agamalian, M.; Melnichenko, Y.B.; Mastalerz, M.; Bustin, R.M.; Radlinski, A.P.; Blach, T.P. Characterization of tight gas reservoir pore structure using USANS/SANS and gas adsorption analysis. *Fuel* **2012**, *95*, 371–385. [[CrossRef](#)]
5. Chen, L.; Jiang, Z.X.; Liu, K.Y.; Tan, J.Q.; Gao, F.L.; Wang, P.F. Pore structure characterization for organic-rich lower silurian shale in the upper yangtze platform, south China: A possible mechanism for pore development. *J. Nat. Gas Sci. Eng.* **2017**, *46*, 1–15. [[CrossRef](#)]
6. Li, P.; Zheng, M.; Bi, H.; Wu, S.T.; Wang, X.R. Pore throat structure and fractal characteristics of tight oil sandstone: A case study in the Ordos Basin, China. *J. Pet. Sci. Eng.* **2017**, *149*, 665–674. [[CrossRef](#)]
7. Huang, H.X.; Sun, W.; Ji, W.M.; Zhang, R.H.; Du, K.; Zhang, S.H.; Ren, D.Z.; Wang, Y.W.; Chen, L.; Zhang, X. Effects of pore-throat structure on gas permeability in the tight sandstone reservoirs of the Upper Triassic Yanchang formation in the Western Ordos Basin, China. *J. Pet. Sci. Eng.* **2018**, *162*, 602–616. [[CrossRef](#)]
8. Nie, R.S.; Zhou, J.; Chen, Z.X.; Liu, J.C.; Pan, Y. Pore structure characterization of tight sandstones via a novel integrated method: A case study of the Sulige gas field, Ordos Basin (Northern China). *J. Asian Earth Sci.* **2021**, *213*, 104739. [[CrossRef](#)]
9. Guo, X.B.; Huang, Z.L.; Zhao, L.B.; Han, W.; Ding, C.; Sun, X.W.; Yan, R.T.; Zhang, T.H.; Yang, X.J.; Wang, R.M. Pore structure and multi-fractal analysis of tight sandstone using MIP, NMR and NMRC methods: A case study from the Kuqa depression, China. *J. Pet. Sci. Eng.* **2019**, *178*, 544–558. [[CrossRef](#)]
10. Li, Y.; Wang, Z.S.; Pan, Z.J.; Niu, X.L.; Yu, Y.; Meng, S.Z. Pore structure and its fractal dimensions of transitional shale: A cross-section from east margin of the Ordos Basin, China. *Fuel* **2019**, *241*, 417–431. [[CrossRef](#)]
11. Wang, W.; Zhao, X.X. Study on characteristics parameters of coal core structure on fractal theory. *J. Henan Univ. (Nat. Sci.)* **2023**, *53*, 729–737.
12. Zhang, C.; Guan, P.; Zhang, J.H.; Liang, X.W.; Ding, X.N.; You, Y. A review of the progress on fractal theory to characterize the pore structure of unconventional oil and gas reservoirs. *Acta Sci. Nat. Universitatis Pekin.* **2023**, *59*, 897–908.
13. Mayo, S.; Josh, M.; Nesterets, Y.; Esteban, L.; Pervukhina, M.; Clennell, M.B.; Maksimenko, A.; Hall, C. Quantitative micro-porosity characterization using synchrotron micro-CT and xenon K-edge subtraction in sandstones, carbonates, shales and coal. *Fuel* **2015**, *154*, 167–173. [[CrossRef](#)]
14. Ren, D.Z.; Zhou, D.S.; Liu, D.K.; Dong, F.J.; Ma, S.W.; Huang, H. Formation mechanism of the Upper Triassic Yanchang Formation tight sandstone reservoir in Ordos Basin—Take Chang 6 reservoir in Jiyuan oil field as an example. *J. Pet. Sci. Eng.* **2019**, *178*, 497–505. [[CrossRef](#)]

15. Wu, Y.P.; Liu, C.L.; Ouyang, S.Q.; Luo, B.; Zhao, D.D.; Sun, W.; Sarwar Awan, R.; Lu, Z.D.; Li, G.X.; Zang, Q.B. Investigation of pore-throat structure and fractal characteristics of tight sandstones using HPMI, CRMI, and NMR methods: A case study of the lower Shihezi Formation in the Sulige area, Ordos Basin. *J. Pet. Sci. Eng.* **2022**, *210*, 110053. [[CrossRef](#)]
16. Nooruddin, H.A.; Hossain, M.E.; Al-Yousef, H.; Okasha, T. Comparison of permeability models using mercury injection capillary pressure data on carbonate rock samples. *J. Pet. Sci. Eng.* **2014**, *121*, 9–22. [[CrossRef](#)]
17. Huang, H.X.; Chen, L.; Sun, W.; Xiong, F.Y.; Ji, W.; Jia, J.K.; Tang, X.L.; Zhang, S.H.; Gao, J.W.; Luo, B. Pore-throat structure and fractal characteristics of Shihezi formation tight gas sandstones in the Ordos Basin, China. *Fractals* **2018**, *26*, 1–22. [[CrossRef](#)]
18. Liu, W.; Lu, S.F.; Wang, M.; Zhang, S.X.; Liu, Y.; Zhou, N.W.; Guan, Y.; Wang, H.L. Overall pore characterization of tight sandstone reservoir space and its significance: A case study of the outer expansion area of Long 26 in Longhupao oilfield, Songliao Basin. *J. Northeast. Pet. Univ.* **2018**, *42*, 41–51.
19. Mandelbrot, B.B. *The Fractal Geometry of Nature*; Freeman: San Francisco, CA, USA, 1983.
20. Zhang, Z.; Weller, A. Fractal dimension of pore-space geometry of an Eocene sandstone formation Fractal dimension of pore-space geometry. *Geophysics* **2014**, *79*, 377–387. [[CrossRef](#)]
21. Li, K.; Horne, R.N. Fractal modeling of capillary pressure curves for the Geysers rocks. *Geothermics* **2006**, *35*, 198–207. [[CrossRef](#)]
22. Liu, D.K.; Sun, W.; Ren, D.Z.; Li, C.Z. Quartz cement origins and impact on storage performance in Permian Upper Shihezi Formation tight sandstone reservoirs in the northern Ordos Basin, China. *J. Pet. Sci. Eng.* **2019**, *178*, 485–496. [[CrossRef](#)]
23. Wang, W.G.; Lin, C.Y.; Zhang, X.G. Fractal dimension analysis of pore throat structure in tight sandstone reservoirs of Huagang Formation: Jiaying area of East China Sea Basin. *Fractal Fract.* **2024**, *8*, 374. [[CrossRef](#)]
24. Deng, Y.H. Analysis on differences of petroleum type and geological conditions between two depression belts in China offshore. *Acta Pet. Sin.* **2009**, *30*, 1–8.
25. Dai, L.M.; Li, S.Z.; Lou, D.; Liu, X.; Suo, Y.H.; Yu, S. Numerical modeling of late Miocene tectonic inversion in the Xihu Sag, East China Sea Shelf Basin, China. *J. Asian Earth Sci.* **2014**, *86*, 25–37. [[CrossRef](#)]
26. Suo, Y.H.; Li, S.Z.; Yu, S.; Somerville, I.D.; Liu, X.; Zhao, S.J.; Dai, L.M. Cenozoic tectonic jumping and implications for hydrocarbon accumulation in basins in the East Asia Continental Margin. *J. Asian Earth Sci.* **2014**, *88*, 28–40. [[CrossRef](#)]
27. Liu, J.S.; Zhang, S.P. Natural gas migration and accumulation patterns in the central-north Xihu Sag, East China Sea Basin. *Nat. Gas Geosci.* **2021**, *32*, 1163–1176.
28. Zhang, J.P.; Zhang, T.; Tang, X.J. Basin type and dynamic environment in the East China Sea Shelf Basin. *Acta Geol. Sin.* **2014**, *88*, 2033–2043, (In Chinese with English abstract)
29. Zhang, S.L.; Zhang, J.P.; Tang, X.J.; Zhang, T. Geometry characteristic of the fault system in Xihu sag in East China Sea and its formation mechanism. *Mar. Geol. Quat. Geol.* **2014**, *34*, 87–94, (In Chinese with English abstract) [[CrossRef](#)]
30. Wang, W.G.; Lin, C.Y.; Zhang, X.G.; Dong, C.M.; Ren, L.H.; Lin, J.L. Discussion of seismic diagenetic facies of deep reservoir in the East China Sea Basin. *J. Pet. Sci. Eng.* **2022**, *208*, 109352. [[CrossRef](#)]
31. Zhu, Y.M.; Li, Y.; Zhou, J.; Gu, S.X. Geochemical characteristics of tertiary coal-bearing source rocks in Xihu depression, East China Sea Basin. *Mar. Pet. Geol.* **2012**, *35*, 154–165. [[CrossRef](#)]
32. Wang, W.G.; Lin, C.Y.; Zhang, X.G.; Dong, C.M.; Ren, L.H.; Lin, J.L. Provenance, clastic composition and their impact on diagenesis: A case study of the Oligocene sandstone in the Xihu sag, East China Sea Basin. *Mar. Pet. Geol.* **2021**, *126*, 104890. [[CrossRef](#)]
33. Zhang, Z.; He, X.; Tang, X.; Zhu, H. Structural trap characteristics and reservoir types in Xihu Sag, East China Sea Basin. *Mar. Geol. Front.* **2022**, *38*, 27–35.
34. Zhang, F.; Jiang, Z.X.; Sun, W.; Li, Y.H.; Zhang, X.; Zhu, L.; Wen, M. A multiscale comprehensive study on pore structure of tight sandstone reservoir realized by nuclear magnetic resonance, high pressure mercury injection and constant-rate mercury injection penetration test. *Mar. Pet. Geol.* **2019**, *109*, 208–222. [[CrossRef](#)]
35. Li, A.F.; Ren, X.X.; Wang, G.J.; Wang, Y.Z.; Jiang, K.L. Characterization of pore structure of low permeability reservoirs using a nuclear magnetic resonance method. *J. China Univ. Pet. (Ed. Nat. Sci.)* **2015**, *39*, 92–98.
36. Zhu, W.B.; Zhang, X.H.; Zhou, D.R.; Fang, C.G.; Li, J.Q.; Huang, Z.Q. New cognition on pore structure characteristics of Permian marine shale in the Lower Yangtze Region and its implications for shale gas exploration. *Nat. Gas Ind.* **2021**, *41*, 41–55. [[CrossRef](#)]
37. Folk, R.L.; Andrews, P.B.; Lewis, D.W. Detrital sedimentary rock classification and nomenclature for use in New Zealand. *N. Z. J. Geol. Geophys.* **1970**, *3*, 937–968. [[CrossRef](#)]
38. Xie, X.H.; Deng, H.C.; Fu, M.Y.; Hu, L.X.; He, J.H. Evaluation of pore structure characteristics of four types of continental shales with the aid of low-pressure nitrogen adsorption and an improved FE-SEM technique in Ordos Basin, China. *J. Pet. Sci. Eng.* **2021**, *197*, 108018. [[CrossRef](#)]
39. Xiang, J.; Zhu, Y.M.; Wang, Y.; Chen, S.B.; Jiang, Z.F. Structural deformation and its pore-fracture system response of the Wufeng-Longmaxi shale in the Northeast Chongqing area, using FESEM, gas adsorption, and SAXS. *J. Pet. Sci. Eng.* **2022**, *209*, 109877. [[CrossRef](#)]
40. Peng, S.; Zhang, T.W.; Loucks, R.G.; James, S. Application of mercury injection capillary pressure to mudrocks: Conformance and compression corrections. *Mar. Pet. Geol.* **2017**, *88*, 30–40. [[CrossRef](#)]
41. Mayka, S.; Fernandes, C.P.; da Cunha Neto, J.A.B.; Wolf, F.G.; dos Santos, V.S.S. Characterization of pore systems in seal rocks using nitrogen gas adsorption combined with mercury injection capillary pressure techniques. *Mar. Pet. Geol.* **2013**, *39*, 138–149.

42. Xiao, D.S.; Zheng, L.H.; Xing, J.L.; Wang, M.; Wang, R.; Guan, X.D.; Guo, X.Y. Coupling control of organic and inorganic rock components on porosity and pore structure of lacustrine shale with medium maturity: A case study of the Qingshankou Formation in the southern Songliao Basin. *Mar. Pet. Geol.* **2024**, *164*, 106844. [[CrossRef](#)]
43. Gao, Y.; Wang, M.; Li, Y.Y.; Jiang, Z.X.; Deng, Y.; Qin, J.H. Multi-scale pore structure characterization of lacustrine fine-grained mixed sedimentary rocks and its controlling factors: A case study of Lucaogou Formation in Jimusar Sag. *Energy Fuels* **2023**, *37*, 977–992. [[CrossRef](#)]
44. Teng, J.B.; Qiu, L.W.; Zhang, S.P.; Ma, C.F. Origin and diagenetic evolution of dolomites in paleogene Shahejie Formation lacustrine organic shale of Jiyang depression, Bohai Bay Basin, east China. *Pet. Explor. Dev.* **2022**, *49*, 1251–1265. [[CrossRef](#)]
45. Zhang, Q.P. Study on Microscopic Pore Throat Structure and Grading Evaluation of Chang 7 Tight Sandstone Reservoirs in Jiyuan Area, Ordos Basin. Ph.D. Thesis, Northwest University, Xi'an, China, 2022; pp. 1–15.
46. Hansen, J.P.; Skjeltorp, A.T. Fractal pore space and rock permeability implications. *Phys. Rev. B* **1988**, *38*, 2635–2638. [[CrossRef](#)] [[PubMed](#)]
47. Ma, B.Y.; Hu, Q.H.; Yang, S.Y.; Zhang, T.; Qiao, H.G.; Meng, M.M.; Zhu, X.C.; Sun, X.H. Pore structure typing and fractal characteristics of lacustrine shale from Kongdian Formation in East China. *J. Nat. Gas Sci. Eng.* **2021**, *85*, 1–16. [[CrossRef](#)]
48. Chang, J.Q.; Fan, X.D.; Jiang, Z.X.; Wang, X.M.; Chen, L.; Li, J.T.; Zhu, L.; Wan, C.X.; Chen, Z.X. Differential impact of clay minerals and organic matter on pore structure and its fractal characteristics of marine and continental shales in China. *Appl. Clay Sci.* **2022**, *216*, 106334. [[CrossRef](#)]
49. Li, K.W. Analytical derivation of Brooks-Corey type capillary pressure models using fractal geometry and evaluation of rock heterogeneity. *J. Pet. Sci. Eng.* **2010**, *73*, 20–26. [[CrossRef](#)]

Disclaimer/Publisher's Note: The statements, opinions and data contained in all publications are solely those of the individual author(s) and contributor(s) and not of MDPI and/or the editor(s). MDPI and/or the editor(s) disclaim responsibility for any injury to people or property resulting from any ideas, methods, instructions or products referred to in the content.